Monthly Notices
of the
ROYAL ASTRONOMICAL SOCIETY

MNRAS **494,** 719–735 (2020)
Advance Access publication 2020 March 20

doi:10.1093/mnras/staa751

RELICS: spectroscopy of gravitationally lensed $z \simeq 2$ reionization-era analogues and implications for C III] detections at $z > 6$

Ramesh Mainali [1,2★] Daniel P. Stark,[1] Mengtao Tang [1] Jacopo Chevallard [3] Stéphane Charlot,[4] Keren Sharon [5] Dan Coe,[6] Brett Salmon,[6] Larry D. Bradley,[6] Traci L. Johnson,[5] Brenda Frye,[1] Roberto J. Avila,[6] Sara Ogaz,[6] Adi Zitrin [7] Maruša Bradač [8] Brian C. Lemaux [8] Guillaume Mahler,[5] Rachel Paterno-Mahler,[9] Victoria Strait[8] and Felipe Andrade-Santos[10]

[1]*Steward Observatory, University of Arizona, 933 N Cherry Ave, Tucson, AZ 85721, USA*
[2]*Observational Cosmology Lab, Goddard Space Flight Center, Code 665, Greenbelt, MD 20771, USA*
[3]*Scientific Support Office, Directorate of Science and Robotic Exploration, ESA/ESTEC, Keplerlaan 1, NL-2201 AZ Noordwijk, the Netherlands*
[4]*Institut d'Astrophysique de Paris, Sorbonne Université, UPMC-CNRS, UMR7095, F-75014 Paris, France*
[5]*Department of Astronomy, University of Michigan, 500 Church Street, Ann Arbor, MI 48109, USA*
[6]*Space Telescope Science Institute, 3700 San Martin Drive, Baltimore, MD 21218, USA*
[7]*Physics Department, Ben-Gurion University of the Negev, PO Box 653, Be'er-Sheva 8410501, Israel*
[8]*Department of Physics, University of California, Davis, CA 95616, USA*
[9]*W.M. Keck Science Center, 925 North Mills Avenue, Claremont, CA 91711, USA*
[10]*Harvard–Smithsonian Center for Astrophysics, 60 Garden Street, Cambridge, MA 02138, USA*

Accepted 2020 March 11. Received 2020 February 19; in original form 2019 September 19

ABSTRACT

Recent observations have revealed the presence of strong C III] emission ($EW_{C\,III]} > 20$ Å) in $z > 6$ galaxies, the origin of which remains unclear. In an effort to understand the nature of these line emitters, we have initiated a survey targeting C III] emission in gravitationally lensed reionization-era analogues identified in *Hubble Space Telescope* imaging of clusters from the Reionization Lensing Cluster Survey. Here, we report initial results on four galaxies selected to have low stellar masses ($2–8 \times 10^7$ $M_\odot$) and J_{125}-band flux excesses indicative of intense [O III] + H β emission ($EW_{[O\,III]+H\,\beta} = 500–2000$ Å), similar to what has been observed at $z > 6$. We detect C III] emission in three of the four sources, with the C III] EW reaching values seen in the reionization era ($EW_{C\,III]} \simeq 17–22$ Å) in the two sources with the strongest optical line emission ($EW_{[O\,III]+H\,\beta} \simeq 2000$ Å). We have obtained a Magellan/FIRE (Folded-port InfraRed Echellette) near-infrared spectrum of the strongest C III] emitter in our sample, revealing gas that is both metal poor and highly ionized. Using photoionization models, we are able to simultaneously reproduce the intense C III] and optical line emission for extremely young (2–3 Myr) and metal-poor (0.06–0.08 $Z_\odot$) stellar populations, as would be expected after a substantial upturn in the star formation rate of a low-mass galaxy. The sources in this survey are among the first for which C III] has been used as the primary means of redshift confirmation. We suggest that it should be possible to extend this approach to $z > 6$ with current facilities, using C III] to measure redshifts of objects with IRAC excesses indicating $EW_{[O\,III]+H\,\beta} \simeq 2000$ Å, providing a method of spectroscopic confirmation independent of Ly α.

Key words: galaxies: evolution – galaxies: high-redshift – galaxies: abundances – galaxies: formation – galaxies: ISM – galaxies: dwarf.

★ E-mail: rmainali@email.arizona.edu

1 INTRODUCTION

Over the past decade, our view of galaxies in the early Universe has been revolutionized by deep infrared (IR) imaging campaigns conducted with the *Hubble Space Telescope* (*HST*). These surveys have led to the discovery of a large photometric sample of galaxies at $z > 6$ (e.g. McLure et al. 2013; Bradley et al. 2014; Bouwens et al. 2015b; Finkelstein et al. 2015; Livermore, Finkelstein & Lotz 2017; see Stark 2016 for a review), providing our first window on the sources thought to be responsible for the reionization of intergalactic hydrogen (e.g. Robertson et al. 2013; Bouwens et al. 2015a; Stanway, Eldridge & Becker 2016; Finkelstein et al. 2019). Analysis of the broad-band spectral energy distributions (SEDs) associated with these galaxies reveals a population of galaxies that are compact and have low stellar mass, with large specific star formation rates (sSFRs; e.g. Labbé et al. 2013; Ono et al. 2013; Stark et al. 2013; González et al. 2014; Salmon et al. 2015; Curtis-Lake et al. 2016).

The first insights into the emission line properties have emerged from *Spitzer*/IRAC broad-band photometry, revealing significant flux excesses in bandpasses covering rest-optical lines (Ono et al. 2012; Finkelstein et al. 2013; Labbé et al. 2013; Smit et al. 2014, 2015). The amplitude of the flux excess indicates the presence of extremely large equivalent width (EW) rest-frame optical line emission in some individual cases at $z > 6$ ($\mathrm{EW}_{[\mathrm{O\,III}]+\mathrm{H}\beta} \simeq 1000$–$2000$ Å), as would be expected for galaxies dominated by very young ($\lesssim$10 Myr) stellar populations. In other galaxies, older stellar populations ($\gtrsim$200 Myr) are present, and the [O III] emission lines are less prominent (e.g. Hashimoto et al. 2018; Strait et al. 2020). The typical reionization-era galaxy appears somewhat between these two extremes. Analysis of composite SEDs constructed from galaxies at $z \simeq 7$ (Labbé et al. 2013) reveals a stellar population that powers strong [O III] + Hβ emission ($\mathrm{EW}_{[\mathrm{O\,III}]+\mathrm{H}\beta} \simeq 670$ Å) but is also old enough (50–200 Myr) to have a small Balmer break. While the nebular emission implied by the average SED is less intense than in the individual examples noted earlier, it is still well above the threshold used to define extreme emission line galaxies (EELGs) at lower redshifts ($\mathrm{EW}_{[\mathrm{O\,III}]\lambda5007} > 100$ Å; Amorín et al. 2014), assuming standard [O III]/Hβ ratios for EELGs (Tang et al. 2019). While these EELGs are rare at lower redshifts (e.g. Atek et al. 2011; van der Wel et al. 2011), they become more frequent at $z > 6$ as large sSFRs become typical (Salmon et al. 2015).

In another few years, our view of these early star-forming sources will be advanced by the spectroscopic capabilities on the *James Webb Space Telescope* (*JWST*), providing our first chance to study the nature of the massive stars and the metallicity of the ionized gas in the reionization era. A preview of the type of spectra that *JWST* is likely to observe at $z > 6$ has recently emerged, revealing nebular emission line properties very different from what is common at lower redshifts. Strong C III] emission has been identified in galaxies at $z = 6.03$ (Stark et al. 2015a), $z = 7.51$ (Hutchison et al. 2019), and $z = 7.73$ (Stark et al. 2017). The rest-frame C III] EW is greater than 20 Å in two of the three $z > 6$ galaxies, more than an order of magnitude greater than what is seen typically at $z \simeq 1$–3 (e.g. Shapley et al. 2003; Steidel et al. 2016; Du et al. 2017, 2018; Le Fèvre et al. 2019). Strong nebular C IV emission has been detected in two low-mass $z > 6$ galaxies (Stark et al. 2015b; Mainali et al. 2017; Schmidt et al. 2017), pointing to a hard ionizing spectrum that is usually associated with active galactic nuclei (AGNs) in galaxies at lower redshifts (Hainline et al. 2011; Le Fèvre et al. 2019). Most recently, the nebular N V emission line has been reported in several additional $z > 7$ galaxies (Tilvi et al. 2016; Hu et al. 2017; Laporte et al. 2017; Mainali et al. 2018), requiring an intense radiation field with significant flux of photons more energetic than 77 eV. Many of these sources have IRAC colours that are suggestive of extreme optical line emission ($\mathrm{EW}_{[\mathrm{O\,III}]+\mathrm{H}\beta} \simeq 1000$–$2000$ Å), larger than the typical values inferred at $z \simeq 7$.

The origin of the strong ultraviolet (UV) nebular line emission that we are seeing in $z > 6$ galaxies remains unclear. While the detection of nebular N V likely points to AGN activity, the powering mechanism of the intense ($\mathrm{EW}_{\mathrm{C\,III]}} > 20$ Å) C III] emission is still a matter of debate in the literature. Stark et al. (2017) investigated the spectral properties of the $z = 7.73$ C III] emitter using BEAGLE (Chevallard & Charlot 2016), a flexible tool for modelling stellar and nebular emission in a consistent manner. With the latest version of the Bruzual & Charlot (2003) population synthesis code (Charlot & Bruzual, in preparation) as the input radiation field, they found that the SED and C III] emission could be reproduced by models with the hard ionizing spectrum of a metal-poor ($\simeq$0.1–0.2 $\mathrm{Z}_{\odot}$) stellar population. Similar results were found in Stark et al. (2015a) when fitting the spectrum of the $z = 6.03$ C III] emitter described earlier. A different picture emerges from Nakajima et al. (2018). They explore the range of UV nebular line spectra that can be powered by stellar populations, considering both single-star models using POPSTAR models (Mollá, García-Vargas & Bressan 2009) and binary star models using BPASS (v2; Stanway et al. 2016). Their results show that stellar photoionization is unlikely to power C III] emission with EW > 20 Å, only reaching such large values when C/O ratios are elevated above the solar abundance ratio, or if the stellar population is hotter than predicted by models as might be expected for an extremely top-heavy initial mass function. As these cases are not likely to be the norm, they suggest that C III] emitters with EW > 20 Å are more likely explained by an ionizing spectrum from a mixture of young massive stars and AGNs.

The tension between these two interpretations highlights the challenges we are soon to face once *JWST* begins collecting large spectroscopic samples at $z > 6$. The problem largely reflects how little we know about the extreme UV (EUV) radiation field powered by low-metallicity massive stellar populations in high-redshift galaxies. Current population synthesis models make different predictions for the shape of the EUV radiation field at low metallicity, making it difficult to link the observed nebular line detections to a unique physical picture. If not addressed prior to the launch of *JWST*, there are bound to be large systematic uncertainties in the physical properties derived from spectra at $z > 6$.

Motivated by this shortcoming, attention has begun to focus on characterizing the rest-UV spectra of star-forming galaxies at $z \simeq 1$–3 (e.g. Erb et al. 2010; Stark et al. 2014; Rigby et al. 2015; Amorín et al. 2017; Du et al. 2017; Le Fèvre et al. 2019) and at $z < 0.01$ (e.g. Berg et al. 2016, 2018; Senchyna et al. 2017, 2019). These studies have demonstrated that prominent metal line emission does appear in star-forming galaxies, provided they have both low metallicity and a stellar population weighted towards very young ages. The latter trend is clearly seen in the relationship between C III] EW and [O III] EW. In spite of the strong C III] emission, many of the metal-poor line emitters are found to have sub-solar C/O ratios (Erb et al. 2010; Berg et al. 2016, 2018). These observations can be collectively explained by photoionization models (e.g. Feltre, Charlot & Gutkin 2016; Gutkin, Charlot & Bruzual 2016; Jaskot & Ravindranath 2016; Byler et al. 2018), with intense UV metal line emission requiring the hard radiation field from young low-metallicity stars and the high electron temperature (T_{e}) associated with metal-poor gas.

Of particular interest is the nature of sources with extremely intense C III] emission ($EW_{C\,III]} > 20$ Å), matching the values seen in the first samples at $z > 7$. At intermediate redshifts ($z \simeq 1$–3), there are a small number of galaxies above this threshold (Amorín et al. 2017; Le Fèvre et al. 2019), but they appear very different from the galaxies described earlier, with signatures of low-luminosity AGNs or atypically large C/O ratios. These results are fully consistent with the picture put forward in Nakajima et al. (2018), whereby the stellar radiation field is in most cases incapable of powering the intense line emission we are now observing at $z > 7$. If true, this would imply that low-luminosity AGNs or large C/O ratios are present among reionization-era spectroscopic samples.

However, such conclusions remain premature as our current census of star-forming galaxies is incomplete. While many metal-poor galaxies have been targeted with rest-UV spectroscopy, most lack the extreme optical line emission ($EW_{[O\,III]+H\,\beta} \simeq 2000$ Å) that appears associated with the UV line emitters at $z > 7$. The extremely young stellar populations (1–5 Myr) probed by these galaxies should produce a very intense EUV ionizing spectrum (Tang et al. 2019), yet little is known about the rest-UV spectra that they power. To address this issue, we have initiated a campaign that aims to characterize the range of C III] EWs powered by metal-poor galaxies with large EW optical line emission. In order to efficiently identify EELGs, we apply well-established colour selection techniques (van der Wel et al. 2011; Maseda et al. 2014) to pick out $z \simeq 1.6$–1.8 galaxies with flux excesses in the J_{125} band from strong [O III] + H β emission. To ensure our sample preferentially consists of metal-poor systems, we focus our search on gravitationally lensed galaxies with blue UV colours and low masses in the Reionization Lensing Cluster Survey (RELICS) fields (Coe et al. 2019). The combination of depth and volume probed by RELICS makes it ideal for building samples of low-mass sources with apparent magnitudes bright enough for ground-based spectroscopy. In this paper, we present rest-UV spectra of four lensed EELGs (including two with $EW_{[O\,III]+H\,\beta} \simeq$ 2000 Å), allowing us to test whether the upper bound of the C III] EW distribution in star-forming galaxies extends to $EW_{C\,III]} > 20$ Å. We have obtained a rest-optical spectrum for the most extreme UV line emitter, allowing us to investigate the origin of the line emission in more detail.

This paper is organized into the following sections. We describe our photometric selection method and spectroscopic observations in Section 2. We then discuss the results of our spectroscopic observations in Section 3 and describe the ionized gas conditions and stellar population properties implied by the spectra in Section 4. We then discuss implications for reionization-era studies in Section 5 and close with a brief summary in Section 6. Throughout the paper, we adopt a Λ-dominated, flat universe with $\Omega_\Lambda = 0.7$, $\Omega_M = 0.3$, and $H_0 = 70\,h_{70}$ km s^{-1} Mpc^{-1}. We use solar oxygen abundance of $12 + \log(O/H)_\odot = 8.69$ (Asplund et al. 2009). We quote magnitudes in the AB system and EWs in the rest frame.

2 SPECTROSCOPIC OBSERVATIONS

2.1 Selection of $z \simeq 2$ EELGs in RELICS fields

Our goal is to characterize the range of rest-UV spectra seen in galaxies with moderately low metallicities and extreme EW optical line emission. Recent studies have focused on $z \simeq 2$ EELGs in the CANDELS fields (e.g. Maseda et al. 2014; Tang et al. 2019). Here, we seek to extend these efforts to lower mass and hence lower metallicity EELGs. We thus focus our search on gravitationally lensed galaxies in the 41 cluster fields imaged by *HST* as part of the RELICS program (GO-14096; Coe et al. 2019). The volume covered by this large data set is ideal for identifying highly magnified objects that are bright enough for ground-based spectroscopy ($m_{AB} < 25.5$).

We first use *HST* imaging data to photometrically select our sample. The RELICS program provides *HST*/WFC3 IR imaging data in four filters (F105W, F125W, F140W, and F160W filters) in all 41 clusters. For those clusters lacking existing archival ACS imaging, RELICS also provides *HST*/ACS optical imaging in F435W, F606W, and F814W filters (see Coe et al. 2019 for details). In addition to RELICS program, the data used in this paper comes from the online *HST* archive: GO-12477 (F. High), GO-12755 (J. Hughes), GO-9722 (H. Ebeling), GO-10493 (A. Gal-Yam), GO-10793 (A. Gal-Yam), and GO-14165 (S. Seitz). We then make use of the publicly available photometric catalogue prepared by the RELICS team based on detection images in a weighted sum of ACS and WFC3 images.[1]

To efficiently select EELGs in the RELICS fields, we make use of well-established colour selection criteria that identify the presence of strong [O III] + H β emission in galaxies at $z \simeq 1.57$–1.79 (van der Wel et al. 2011; Maseda et al. 2014; Tang et al. 2019). At these redshifts, both lines are situated in the J_{125} band (F125W). Galaxies with large EW [O III] + H β emission are easily identifiable by the large flux excess that appears in the J_{125} band relative to the adjacent I_{814} (F814W) and H_{160} (F160W) bands. We follow the colour cuts used in van der Wel et al. (2011), selecting sources with $I_{814} - J_{125} > 0.44 + \sigma(I_{814} - J_{125})$ and $J_{125} - H_{160} < -0.44 - \sigma(J_{125} - H_{160})$, where σ refers to the uncertainty in the colour. The amplitude of the J_{125}-band excess can be directly related to the rest-frame EW given by

$$EW = \left(\frac{f_{total} - f_{cont}}{f_{cont}}\right)\frac{W}{1+z}, \quad (1)$$

where W is the effective width of the J_{125} filter, f_{total} is the flux density f_ν in the J_{125} filter, and f_{cont} is the average flux density in the I_{814} and H_{160} filters. The colour cuts described above thus select sources with rest-frame [O III] + H β EW > 500 Å.

We apply the EELG selection criteria in all 41 RELICS clusters, utilizing the broad-band fluxes from the publicly available photometric catalogue prepared by the RELICS team. Most cluster fields have one to two EELGs with typical apparent magnitude of $m_{AB} \sim 25.5$ in the I_{814} band. We focus spectroscopic follow-up on sources that have bright continuum magnitudes ($m_{AB} < 25.5$) and large J_{125}-band excesses implying extremely intense optical line emission.

In this paper, we present observations of four lensed EELGs from the parent sample with 600 Å < [O III] + H β EW < 2000 Å. *HST* imaging postage stamps are shown in Fig. 1, revealing the very compact sizes of each of the four sources. The impact of [O III] + H β emission on the J_{125} band is clearly visible in the SEDs shown in Fig. 2. We provide details of the four sources in Table 1 and discuss each individually below. The magnification provided by the cluster is calculated from lens models prepared by the RELICS team and available to the public.[1] Further details on the lens modelling procedure have been presented in recent RELICS papers (Acebron et al. 2018; Cerny et al. 2018; Cibirka et al. 2018; Paterno-Mahler et al. 2018). In calculating the magnification and

[1] https://archive.stsci.edu/prepds/relics/

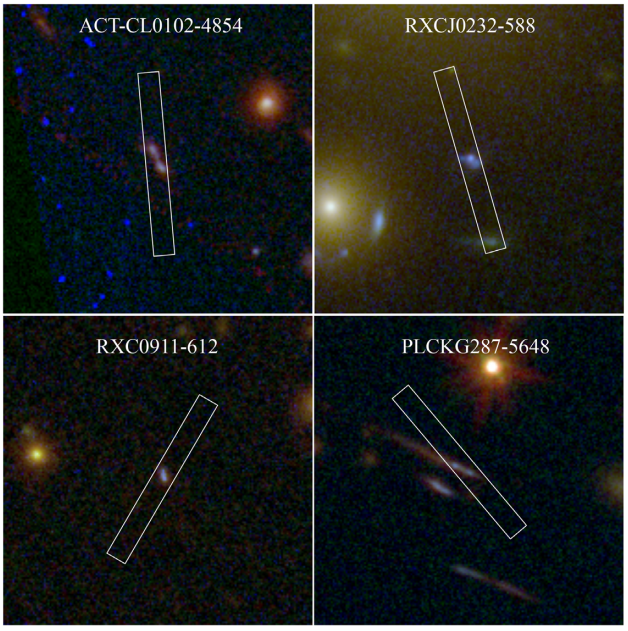

Figure 1. *HST* colour images of the lensed EELGs galaxies presented in this paper. The top of each image shows the cluster name followed by the galaxy name. The size of each image is 10 arcsec × 10 arcsec.

the absolute magnitude, we assume the confirmed spectroscopic redshift presented in Section 3.

RXCJ0232−588 is a compact (r_e = 0.1 arcsec), blue ($\beta = -2.3$) galaxy with a pronounced J_{125}-band flux excess (Fig. 2) indicative of strong rest-optical nebular emission ($EW_{[O\,III]+H\beta} = 1990 \pm 200$ Å). Its apparent optical magnitude is the brightest in our sample ($I_{814} = 23.6$), making it an ideal target for spectroscopy. The RXCJ0232.2−4420 lens model indicates a magnification factor of $\mu = 7.96^{+0.02}_{-1.72}$. After correcting for magnification, we calculate an absolute UV magnitude of $M_{UV} = -18.72^{+0.28}_{-0.02}$.

RXCJ0911−612 is a bright (I_{814} = 25.2) compact galaxy (r_e = 0.1 arcsec) with a prominent J_{125}-band flux excess (Fig. 2), indicating extremely strong optical line emission ([O III] + H β EW = 1850 ± 170 Å). Based on the lens model for RXCJ0911.1+1746, we estimate that the cluster has magnified this object by a factor of $\mu = 3.8^{+0.11}_{-0.13}$. After correcting for the magnification, we find that RXCJ0911−612 has an absolute magnitude of $M_{UV} = -17.92^{+0.02}_{-0.03}$.

PLCKG287−5648 was previously identified as a multiply imaged system by Zitrin et al. (2017) (ID number 2 in their paper). Among the three images, only 2.3 has near-IR imaging coverage necessary for the EELG colour selection. The source is relatively bright (I_{814} = 24.4), has a blue UV slope ($\beta = -1.9$), and shows a slightly extended arc-like structure in the *HST* images (Fig. 1). The J_{125}-band flux excess is evident in the SED (Fig. 2), implying an [O III] + H β EW of 1120 ± 150 Å. Using the cluster lens model, we find that the galaxy is magnified by a factor of $\mu = 13.6^{+0.4}_{-3.2}$. After correcting for this factor, we derive an absolute magnitude of

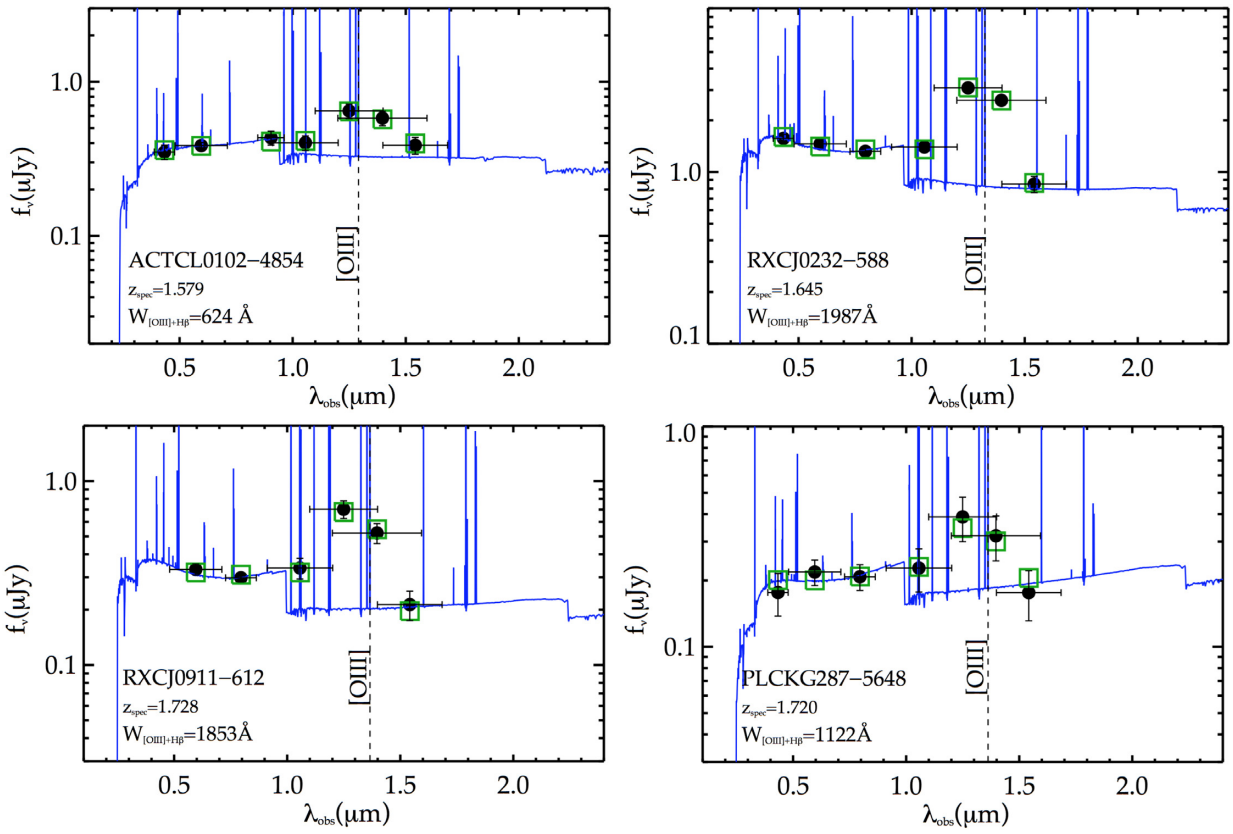

Figure 2. SEDs of four EELGs in our sample. The broad-band flux excesses can be seen in the F125W and F140W filters. The black circles and green squares represent observed and synthetic data points, respectively. The blue curves show the best-fitting SED models inferred using BEAGLE (see Section 4.2). The bottom left of each panel shows the object ID, spectroscopic redshift, and [O III] + H β EW as implied by the J_{125}-band flux excess.

Table 1. Properties of gravitationally lensed EELGs presented in this paper. From left to right, the columns denote the cluster name, object ID (taken from RELICS catalogue), $z_{\rm spec}$, right ascension (RA) and declination (Dec.) of object, I_{814}-band magnitude, UV slope, [O III] + H β EWs (rest frame) implied by the J_{125}-band photometric excess, and magnification factor of the source.

Cluster	ID	$z_{\rm spec}$	RA	Dec.	I_{814}	UV slope (β)	EW$_{\rm [O\,III]+H\,\beta}$ (Å)	Magnification factor (μ)
ACTCL0102−49151	4854	1.579	01:03:04.619	−49:17:04.62	24.2	−1.9	620 ± 220	$1.41^{+0.12}_{-0.12}$
RXCJ0232.2−4420	588	1.645	02:32:16.124	−44:20:55.72	23.6	−2.3	1990 ± 200	$7.96^{+0.02}_{-1.72}$
PLCKG287.0+32.9	5648	1.720	11:50:52.800	−28:06:03.24	24.4	−1.9	1120 ± 150	$13.6^{+0.4}_{-3.2}$
RXCJ0911.1+1746	612	1.727	09:11:09.912	17:46:54.84	25.2	−2.2	1850 ± 170	$3.8^{+0.1}_{-0.1}$

Table 2. Details of LDSS3 and IMACS spectroscopic observations. From left to right, the columns denote the cluster name, cluster redshift, mask name, RA and Dec. of mask centre, instrument, date of observations, positional angle (PA) of masks, and total exposure time per mask. Further details are provided in Section 2.

Cluster	Cluster redshift	Mask	Mask centre		Instrument	Dates	PA (deg)	$t_{\rm exp}$ (ks)
			RA	Dec.				
RXCJ0232.2−4420	0.2836	rxc0232	02:32:17.683	−44:20:35.67	LDSS3	2016 November 27	196	7.2
RXCJ0911.1+1746	0.5049	rxc0911	09:10:56.692	17:49:06.94	IMACS	2019 March 6–7	−30	20.4
PLCKG287.0+32.9	0.3900	p287	11:51:04.021	−28:04:56.58	IMACS	2019 March 6–7	40	13.2
ACTCL0102−49151	0.8700	elgordo	01:02:58.980	−49:16:01.52	LDSS3	2016 August 2	185	7.2

$M_{\rm UV} = -17.14^{+0.29}_{-0.02}$, more than an order of magnitude less than $M^{\star}_{\rm UV}$ at $z \simeq 2$ (e.g. Alavi et al. 2016).

ACTCL0102−4854 is the second brightest source in our sample ($I_{814} = 24.8$) but has a less pronounced J_{125}-band flux excess than the three sources discussed earlier. While still an EELG, its optical line EW is the weakest in our spectroscopic sample (EW$_{\rm [O\,III]+H\,\beta} = 620 \pm 220$ Å). The source shows a slightly elongated structure (Fig. 1) with a blue UV slope ($\beta = -1.9$). We compute a magnification factor of $\mu = 1.41^{+0.12}_{-0.12}$ using the RELICS lens model for ACTCL0102−49141. Applying this magnification factor to the apparent magnitude, we compute an absolute UV magnitude of $M_{\rm UV} = -19.84^{+0.14}_{-0.14}$, making ACTCL0102−4854 the most luminous object in our sample.

2.2 Optical spectroscopy

The four EELGs described earlier were observed over three Magellan observing runs between 2016 and 2019. For the first two observing runs, we used the Low Dispersion Survey Spectrograph 3 (LDSS3) spectrograph on the Magellan Clay telescope, targeting the cluster fields with ACTCL0102−4854 and RXCJ0232−588. These observing runs formed part of a larger spectroscopic survey of lensed galaxies in the RELICS fields using University of Michigan and University of Arizona time allocation that we will present in a future paper (Mainali et al. , in preparation). In our most recent run, we used the Inamori-Magellan Areal Camera and Spectrograph (IMACS; Dressler et al. 2011) on the Magellan Baade telescope to target the fields with RXCJ0911−612 and PLCKG287−5648. Next, we first describe the LDSS3 observations and reduction, and then detail the same for IMACS. Details of the observing set-up are provided in Table 2.

We utilize LDSS3 in multi-object mode, designing two masks targeting the ACTCL0102 and RXCJ0232 fields. In addition to the EELGs discussed in Section 2.1, we include other gravitationally lensed systems and cluster members. Slit widths were set to 1.0 arcsec, while the typical slit lengths were 6.0 arcsec. We used the VPH-ALL grism (400 lines mm^{-1}) with no order blocking filter, providing continuous spectral coverage from 4000 to 10 000 Å with a spectral resolution of 7.7 Å. This set-up allows us to detect C III] throughout the redshift range selected by our colour selection. For sources at $z < 1.68$, we should also be able to confirm redshifts by detection of the [O II] doublet. We observed the ACTCL0102 field on 2016 August 2 and the RXCJ0232 field on 2016 November 27. Both masks were observed for 2 h with typical seeing of 0.7 arcsec.

The LDSS3 data were reduced using the publicly available Carnegie Observatories System for MultiObject Spectroscopy pipeline.[2] We obtained bias fields during each afternoon prior to observations. Flat-fields were obtained using quartz lamps, and arcs were observed using HeNeAr lamps. Both flat-fields and arcs were taken during the nights prior to observing each field. The pipeline performs bias subtraction, flat-fielding, and a wavelength calibration using the comparison arcs. The wavelength solutions have typical rms of 1.5 Å. The pipeline does sky subtraction using the optimal method from Kelson (2003) before outputting the final 2D spectra. Finally, the 1D spectrum is produced using a boxcar extraction with an aperture of 1.1 arcsec (6 pixels). The final 1D error spectrum is extracted from the output 2D error spectrum generated by the pipeline. We observed a standard star to compute instrumental response across the detector. The absolute flux calibration is then obtained from the known continuum magnitudes of several slit stars that are placed on our masks. The LDSS3 spectra provide a median line flux limit (3σ) of 1.3×10^{-17} erg cm^{-2} s^{-1} in the wavelength range 5000–6000 Å. This flux limit provides rest-frame EW limits (3σ) as low as ∼3–5 Å for C III] over the same wavelength range.

We observed the PLCKG287 and RXCJ0911 fields using IMACS in multi-object mode. As with the LDSS3 observations, we designed slit masks that include a mixture of the EELGs, candidate lensed galaxies, and cluster galaxy members. For the PLCKG287 mask, we also placed a slit on one of the other images of EELG PLCKG287−5648 (source 2.2 using the Zitrin et al. 2017 nomen-

[2] http://code.obs.carnegiescience.edu/cosmos

clature). We used the 300 lines mm^{-1} grating blazed at an angle of 17.5° with the *f*/2 camera. The grating is optimized to provide wavelength coverage from 3900 to 8000 Å, covering C III] and other UV metal lines in the expected wavelength range. We used a slit width of 1.0 arcsec that provided a spectral resolution of 6.7 Å.

Both masks were observed on 2019 March 6–7. Conditions were clear throughout the observations with an average seeing of 0.7 arcsec. Because of the fainter continuum magnitudes of the EELGs in these fields, we obtained longer exposure times (∼3.5–5.5 h) in order to reach sufficient depth to detect emission lines with rest-frame EWs as low as ∼3–5 Å. The data were reduced using the same pipeline and procedure as described earlier. Similar to the LDSS3 spectra, the absolute calibration is performed using continuum magnitudes of slit stars placed on our masks. We reached median line flux sensitivities (3σ) of 7.2 × 10^{-18} erg cm^{-2} s^{-1} (RXCJ0911−612) and 9.6 × 10^{-18} erg cm^{-2} s^{-1} (PLCKG287−5648) in the wavelength range (5000–6000 Å) where C III] is situated, enabling constraints to be placed on lines with rest-frame EWs as low as ∼5 Å.

2.3 Near-IR spectroscopy of RXCJ0232−588

We recently initiated near-IR spectroscopic follow-up of the EELGs, targeting RXCJ0232−588 with Folded-port InfraRed Echellette (FIRE; Simcoe et al. 2013) on the Magellan Baade telescope. Spectra in the near-IR are required to detect strong rest-optical nebular lines (i.e. [O II], H β, [O III], H α) that constrain the physical conditions of the ionized gas, allowing us to better understand the properties most important for regulating the strength of the UV metal lines. Observations were obtained on 2018 September 2. FIRE was operated in echelle mode, providing spectral coverage between 0.82 and 2.51 μm. The observations were carried out using a slit width of 1.0 arcsec, resulting in a resolving power of $R = 3600$. RXCJ0232−588 was observed for a total on-source integration time of 3 h. Throughout the observations, the conditions were excellent with an average seeing of 0.5 arcsec.

The spectrum of RXCJ0232−588 was reduced using standard routines in the FIREHOSE data reduction pipeline.[3] The pipeline uses lamp and sky flats for flat-fielding. 2D sky models are then iteratively calculated following Kelson (2003). The wavelength solutions are provided by fitting OH skylines in the spectra. Flux calibration and telluric corrections to the data are applied using A0V star observations. Finally, the 1D spectrum was extracted using a boxcar with aperture of 0.9 arcsec (15 pixels).

3 RESULTS

Here, we present the results from our spectroscopic observations of lensed EELGs. In all cases, the spectra confirm the redshifts to lie in the range ($1.57 < z < 1.79$) predicted by the J_{125}-band excess. We first present redshift measurements and constraints on C III] and other UV lines (Section 3.1) before discussing the rest-optical lines detected in the FIRE spectrum of RXCJ0232−588 (Section 3.2).

[3] wikis.mit.edu/confluence/display/FIRE/FIRE+Data+Reduction

3.1 Rest-UV spectra: probing C III] emission in EELGs

3.1.1 RXCJ0232−588 ($EW_{[O\,III]+H\beta} = 1990$ Å)

The LDSS3 spectrum of RXCJ0232−588 covers rest-frame wavelengths between 1654 (1523) and 3891 (3584) Å assuming the extrema of the redshift range predicted by the *J*-band excess, $1.57 < z < 1.79$. The spectrum shows four emission lines at 4406.6, 4980.1, 5046.3, and 9861.2 Å together with a continuum trace between 4200 and 9200 Å (Fig. 3). We derive a redshift solution of $z = 1.645$ with the lines corresponding to O III] λ1666, Si III] λ1883, and the blended C III] λ1908 and [O II] λ3728 doublets. We also identify a tentative detection (S/N = 1.9) at 5004.1 Å. This corresponds to the location of Si III] λ1892 component (Fig. 3). We do not see emission from O III] λ1661. The upper limit on the non-detection implies O III] doublet ratio of 1666:1661 > 1 (at 3σ). This limit is fully consistent with the observed doublet ratio in similar galaxies (e.g. Erb et al. 2010; Stark et al. 2014; Berg et al. 2019).

We measure line fluxes of each emission feature by directly integrating fluxes after subtracting continuum near each line. We then correct for the small aperture losses via methods described in previous papers (e.g. Stark et al. 2014). Briefly, we convolve the *HST* image with the ground-based seeing and calculate the fraction of the object falling on the slit. We then do the same for the slit star that was used to compute the absolute flux calibration. The ratio of the object and star slit losses gives the factor by which we must correct our measured line fluxes, accounting for the spatial extent of the sources. In the galaxies considered in this paper, the sizes are sufficiently compact that this correction factor is negligible. In the case of RXCJ0232−588, we derive a very small correction factor of 1.05, consistent with its compact nature. We finally compute the EWs, dividing the emission line fluxes by the continuum flux level near the line of interest. The continuum is derived from the spectrum when it is detected confidently (S/N > 10) in a window of 200 Å surrounding the emission line in question. In cases where the continuum is not detected at the desired wavelength, we use the value implied by the best-fitting population synthesis model (see Section 4.2).

The rest-UV line measurements of RXCJ0232−588 are presented in Table 3. It is clear from the table that this source is one of the most extreme UV line emitters known outside the reionization era. In particular, the spectrum clearly shows a strong C III] emission feature with $EW_{C\,III]} = 21.7 \pm 2.8$ Å. This is larger than the 20 Å threshold that has been suggested as a signpost for photoionization from AGN or super-solar C/O ratios (Nakajima et al. 2018), although we note that the EW uncertainty is such that this source could have a C III] EW just below 20 Å. As we will show in Section 5, RXCJ0232−588 is consistent with an extension of the relationship between C III] and [O III] EW derived from a compilation of sources in the literature, with the largest C III] strengths seen in galaxies with the most extreme optical line emission. The other detected UV lines are also very strong ($EW_{O\,III]\lambda1666} = 3.8 \pm 1.3$ Å and $EW_{Si\,III]\lambda1883} = 4.9 \pm 1.2$ Å), with values among the largest seen in metal-poor star-forming galaxies (e.g. Vanzella et al. 2016a, 2017; Senchyna et al. 2017; Berg et al. 2018, 2019). The blended [O II] doublet is detected with $EW_{[O\,II]} = 100 \pm 11$ Å, similar to the strengths seen in other $z \simeq 2$ EELGs (Tang et al. 2019). We will present the rest-optical spectrum of this source in Section 3.2, providing a more detailed picture of the physical conditions of the nebular gas, a topic we will come back to in Section 4.1.

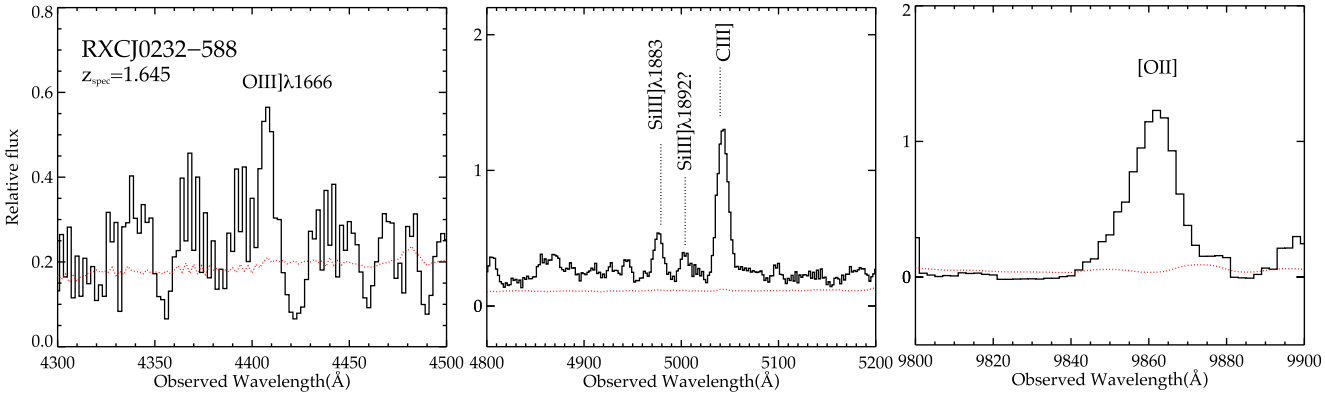

Figure 3. Magellan/LDSS3 spectrum of RXCJ0232−588 showing O III] λ1666 line (left), Si III] λ1883 and blended C III] λλ1907,1909 (middle), and blended [O II] λλ3727,3729 (right). The black curve represents flux level and red dotted line represents 1σ error level in each panel.

Table 3. Magellan/LDSS3 and Magellan/IMACS emission line measurements of four EELGs presented in this paper. The upper limits are quoted at 3σ.

Object	Line	λ_{rest} (Å)	λ_{obs} (Å)	Flux (10^{-17} erg s^{-1} cm^{-2})	EW (Å)
RXCJ0232−588	O III]	1666.15	4406.6	2.7 ± 0.9	3.8 ± 1.3
	Si III]	1882.71	4980.1	2.6 ± 0.6	4.9 ± 1.2
	Si III]	1892.03	5004.1	1.1 ± 0.6	2.1 ± 1.2
	C III]	1907.71	5046.3	10.9 ± 1.2	21.7 ± 2.8
	[O II]	3728.6	9861.2	8.8 ± 0.8	99.8 ± 11.2
PLCKG287−5648	C IV	1549	–	<1.2	<6.6
	He II	1640.42	–	<1.1	<5.5
	O III]	1666.15	–	<1.1	<5.5
	C III]	1907.71	5189.8	0.9 ± 0.2	4.8 ± 1.2
RXCJ0911−612	C IV	1549	–	<0.8	<5.9
	He II	1640.42	–	<0.7	<7.3
	O III]	1666.15	–	<0.7	<7.3
	C III]	1907.71	5204.4	1.7 ± 0.3	16.9 ± 3.2
ACTCL0102−4854	C III]	1907.71	–	<1.1	<4.0
	[O II]	3728.6	9615.4	4.5 ± 0.3	59.2 ± 5.7

3.1.2 RXCJ0911−612 ($EW_{[O\,III]+H\beta}$ = 1850 Å)

The optical spectrum of RXCJ0911−612 spans 1556 (1434) to 3502 (3226) Å in the rest frame, corresponding to the extrema of the redshift range predicted by the *J*-band excess, $1.57 < z < 1.79$. In this wavelength window, we expect C III] to be our best probe of the redshift. Over the redshift range predicted by the J_{125}-band excess, C III] is expected to be situated at observed wavelengths between 4903 and 5322 Å. We scan this wavelength window for lines and detect a confident (S/N = 6.6) emission feature at 5204.4 Å (Fig. 4). We identify this as the blended C III] doublet at a redshift of $z = 1.728$. To calculate this redshift, we assume a rest-frame wavelength of 1907.709 Å for the unresolved doublet (see Erb et al. 2010). We detect no other confident (>5σ) emission features throughout the spectrum, consistent with expectations that C III] should be the brightest line in this portion of the spectrum.

We measure the flux and upper limits of emission lines using the same procedure described earlier. The integrated flux of the combined C III] doublet is $1.7 \pm 0.3 \times 10^{-17}$ erg cm^{-2} s^{-1}. The aperture correction relative to the slit star is again very small (1.08×), not surprising given the compact size of RXCJ0911−612. Using the continuum measured from the SED, we compute the rest-frame EW of C III] and place upper limits on the other lines. Similar to RXCJ0232−588, we find a value ($EW_{C\,III]} = 16.9 \pm 3.2$ Å) that is similar to what has been seen at $z > 6$. Our measurements are presented in Table 3.

3.1.3 PLCKG287−5648 ($EW_{[O\,III]+H\beta}$ = 1120 Å)

The IMACS spectrum of PLCKG287−5648 covers the same rest-wavelength window as for RXCJ0911−612. We expect C III] emission to be the strongest line in the spectrum. We search for line emission in the observed wavelength window where C III] is expected to lie (4903–5322 Å). As shown in Fig. 5 (right-hand panel, blue), we detect a 3.2σ emission feature at an observed wavelength of 5189.8 Å. If this is indeed C III], we should see emission at the same wavelength in PLCKG287−5404, another lensed image of the same galaxy (see discussion in Section 2.1). As is apparent in Fig. 5 (right-hand panel, green), an emission line is seen at the same wavelength in the second image. By median stacking the two spectra (Fig. 5, left-hand panel), we detect the

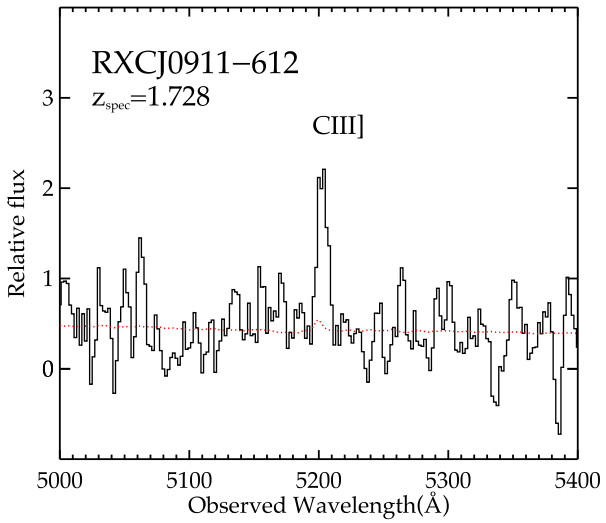

Figure 4. Magellan/IMACS spectrum of RXCJ0911−612 showing detection of blended C III] λλ1907,1909. The black curve in the plot represents flux level and red dotted curve denotes 1σ error level in the spectrum.

emission feature at higher significance (S/N = 4.6). We classify the detected feature as C III] emission at a redshift of $z = 1.720$, consistent with the redshift range implied by the strong J_{125}-band excess. We do not detect any other emission lines in the IMACS spectrum, as expected given the faint continuum of this EELG.

Following the same procedures we have described earlier, we measure a flux of $9.1 \pm 2.0 \times 10^{-18}$ erg cm^{-2} s^{-1} for the C III] line in the stacked spectrum. After making a small correction (1.21×) for slit losses (relative to the slit star used for flux calibration), we compute the rest-frame EW. For this source, we use the continuum derived from the SED. The resulting value ($EW_{C\,III]} = 4.8 \pm 1.1$ Å) is considerably lower than that in the EELGs described earlier with more intense [O III] emission. Looking at the relationship between C III] and [O III] + H β EW (see Section 5), we see that the measured C III] strength in PLCKG287−5648 is lower than most sources with $EW_{[O\,III]+H\,\beta} \simeq 1000$ Å. Further follow-up in the near-IR should help clarify the origin of the scatter in this relationship.

3.1.4 ACTCL0102−4854 ($EW_{[O\,III]+H\,\beta} = 620$ Å)

The LDSS3 spectrum of ACTCL0102−4854 covers rest-frame wavelengths between 1654 (1523) and 3891 (3584) Å, assuming the extrema of the redshift range predicted by the *J*-band excess, $1.57 < z < 1.79$. We first scan for lines in the observed wavelength range where [O II] is expected (9583–10 402 Å). A strong emission feature is readily apparent at 9615.4 Å (Fig. 6). This is consistent with a redshift of $z = 1.579$, assuming a rest wavelength of 3728.6 Å for the unresolved doublet. This rest wavelength is calculated assuming a doublet flux ratio consistent with that seen in $z \simeq 2$ galaxies (e.g. Sanders et al. 2016). At this redshift, we would expect C III] to appear at 4920 Å. No emission feature is seen in the vicinity of this wavelength, allowing us to place an upper limit on the line flux. The other rest-UV lines (C IV, He II, and O III]) are all blueward of the LDSS3 spectral coverage, so we cannot put constraints on their strength.

We derive the line flux of [O II] using the same methods as we described for the other three EELGs. The integrated line flux is $4.4 \pm 0.3 \times 10^{-17}$ erg cm^{-2} s^{-1}. We correct this flux by a very small factor (1.14×), accounting for the excess slit losses of ACTCL0102−4854 relative to the stars used for flux calibration. We finally calculate the rest-frame EW, using the continuum predicted near [O II] from the SED model. The resulting value ($EW_{[O\,II]} = 59.2 \pm 5.7$ Å) is within the range seen in similar strength [O III] emitters (Tang et al. 2019). The absence of C III] suggests an upper limit of $EW_{[C\,III]} = 4.0$ Å, slightly weaker than average for galaxies with similar $EW_{[O\,III]+H\,\beta}$. We present line measurements and upper limits in Table 3.

3.2 Rest-optical spectroscopy

The FIRE spectrum of RXCJ0232−588 reveals 10 unique emission features ([O II]λλ3727, 3729, [Ne III] λ3869, [Ne III] λ3968, H ϵ, H δ, H γ, H β, [O III] λλ4959, 5007). Using the wavelength centroid calculated from the highest signal-to-noise nebular lines (H β, [O III] λλ4959, 5007), we estimate a redshift of $z = 1.6448$, consistent with the spectroscopic redshift derived from the LDSS3 data. The line widths are narrow (full width at half-maximum = 106.4 km s^{-1}, corrected for instrumental resolution). To compute line fluxes, we need to establish the absolute flux scale in the FIRE spectrum. Since the [O II] emission line is also detected in our optical spectrum (see Section 3.1), we can bootstrap the flux calibration of FIRE to that of LDSS3, the latter of which is determined with more confidence owing to the availability of slit stars observed simultaneously with the science spectra. This process takes into account flux calibration uncertainty in both FIRE and LDSS3 data whenever measuring line ratios that involve emission lines from the two spectra.

In Fig. 7, we present the 1D spectrum in the vicinity of the strong rest-frame optical emission lines. The majority of these lines are not significantly affected by skylines, enabling robust measurements of the integrated line flux. We obtain these measurements using the MPFITPEAK routine in IDL, and corresponding errors are calculated using the error spectrum. Looking at the lower right-hand panel in Fig. 7, it is clear that H α is coincident with a sky feature. While the line is clearly detected, residuals from the sky subtraction make a reliable flux measurement challenging. We will discuss this further below. Since the stellar continuum is undetected in the FIRE spectrum, we compute EWs using the continuum derived from our best-fitting broad-band SED models (see Fig. 2 and Section 4.2). The measurement of line fluxes and corresponding EWs are presented in Table 4.

We characterize the impact of nebular attenuation using the observed flux ratios of the hydrogen Balmer lines. Since H α is partially contaminated by a skyline, we consider the ratio of H γ and H β. For case B recombination, no dust, and an electron temperature of 10^4 K, we expect to see $F_{H\,\gamma}/F_{H\,\beta} = 0.468$ (Osterbrock & Ferland 2006). The presence of dust will act to decrease this ratio relative to the theoretical value. The observed flux ratio in the FIRE spectrum ($F_{H\,\gamma}/F_{H\,\beta} = 0.48 \pm 0.06$) thus suggests little to no dust attenuation, consistent with the very blue UV continuum slope ($\beta = -2.3$) seen in the *HST* imaging (Fig. 2). In the analysis that follows, we assume that the source is not significantly reddened ($E(B-V)_{neb} = 0.00$), similar to other EELGs with similar [O III] EW (Tang et al. 2019). In our analysis that follows in Section 4, we thus take the observed line ratios as those intrinsic to the source. Whenever required, we use the H α line strength implied by scaling the observed H β flux by the theoretical flux ratio ($F_{H\,\alpha}/F_{H\,\beta} = 2.86$) for case B recombination and 10^4 K gas (Osterbrock & Ferland 2006).

The FIRE spectrum confirms the extreme emission lines implied by the photometry, revealing [O III] λ5007 with EW = 1426 ± 57 Å

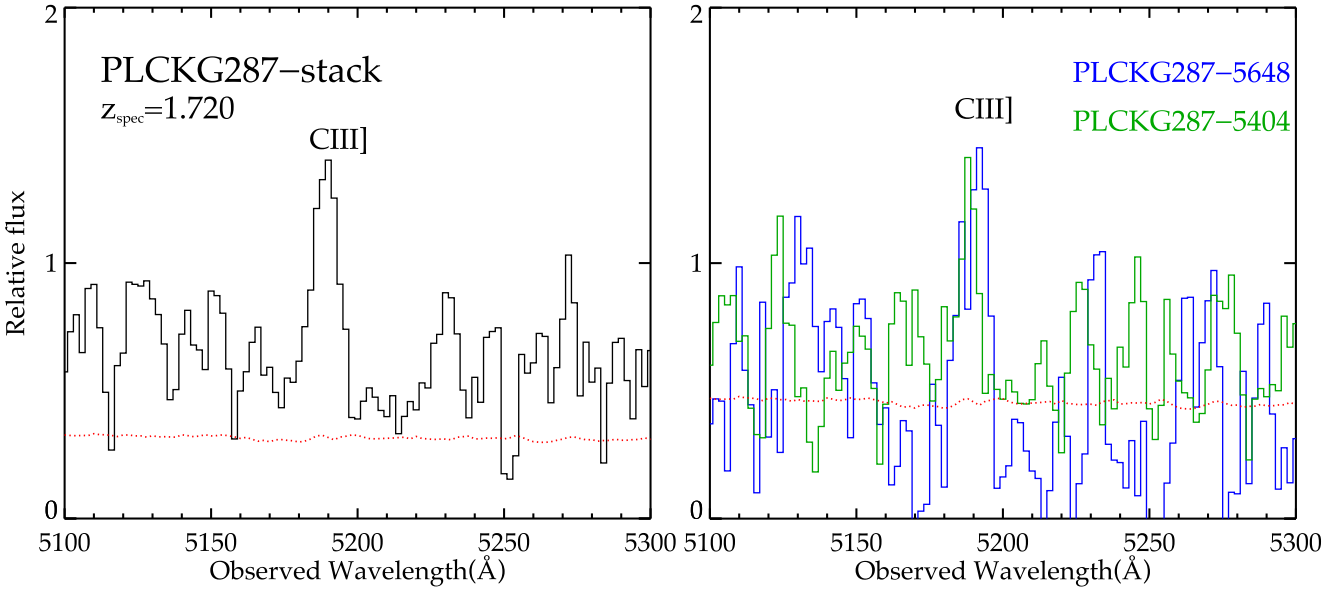

Figure 5. Magellan/IMACS spectra of PLCKG287−5648 and PLCKG287−5404, lensed images of the same galaxy. The left-hand panel represents the stack of the two spectra where a blended C III] λλ1907,1909 line is visible. The right-hand panel shows the spectrum of PLCKG287−5648 in blue and PLCKG287−5404 in green. The C III] emission feature is individually detected in each lensed image.

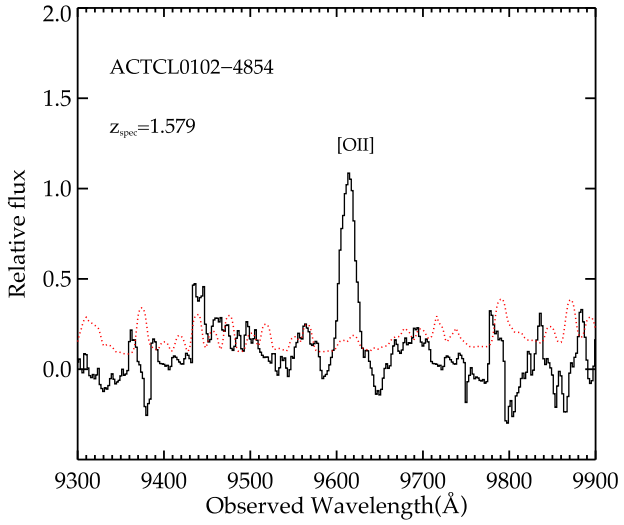

Figure 6. Magellan/LDSS3 spectrum of ACTCL0102−4854. The black curve and red dotted line represent flux and 1σ uncertainty, respectively. A blended [O II] λλ3727,3729 is visible as a single prominent emission feature in the spectrum.

and Hβ with EW = 325 ± 23 Å (Table 4). These values place RXCJ0232−588 among the most extreme optical line emitters known at high redshift (e.g. Tang et al. 2019), likely implying a very young stellar population (see Section 4.2). The spectrum constrains numerous emission line ratios that are sensitive to the abundance and ionization state of the gas. We list and define these in Table 5.

4 ANALYSIS

In this section, we explore the properties of the four gravitationally lensed EELGs described in Section 3. We first explore the properties of RXCJ0232−588 in detail, leveraging the large number of emission lines that we have detected in our spectra of this source. We then consider the properties of our full sample, as implied by photoionization models. In addition to constraining the gas conditions, these results reveal the population has low stellar masses and young stellar populations, as would be expected for galaxies that have recently undergone a substantial upturn in their star formation.

4.1 Ionized gas properties of a reionization-era analogue with intense UV metal line emission

We use the emission line spectrum of RXCJ0232−588 to investigate the ionized gas properties of one of the few known low-mass star-forming galaxies that powers C III] as strong as that found at $z > 6$. In addition to constraining the metallicity and ionization conditions of the galaxy, we seek to put this C III] emitter in a broader context, comparing the observed line ratios to those of more massive and older star-forming systems that are far more typical at $z \simeq 2$. We use the insight gained from this analysis to comment on the likely powering mechanism of the C III] emission.

We first estimate the gas-phase oxygen abundance using the direct electron temperature (T_e) method. While we do not detect the [O III] λ4363 auroral line, we do secure detection of O III] λ1666, another auroral line commonly used to derive T_e. We use PYNEB PYTHON package (version 1.1.8; Luridiana, Morisset & Shaw 2015) to calculate T_e([O III]) from the observed flux ratio of O III] λ1666 and [O III] λ5007. We fix the electron density to n_e = 80 cm^{-3}, as implied by the [O II] doublet ratio (Table 5). Since the Balmer decrement suggests negligible nebular attenuation (Section 3.2), we use the observed ratio of O III] λ1666 and [O III] λ5007 as intrinsic, propagating the errors on the Balmer decrement through to the temperature. With these assumptions, we derive an electron temperature of 16500 ± 2400 K for the O^{2+} zone. We next calculate T_e([O II]) following the relation given in Pérez-Montero (2017) that estimates T_e([O II]) using T_e([O III]) and an electron density (n_e). This gives a temperature of T_e([O II]) = 14800 ± 2100 K for the O^+ zone. Using these temperatures in O^+ and O^{2+} zones, we calculate O^+/H^+ and O^{2+}/H^+ from PYNEB. Combining the two ionic

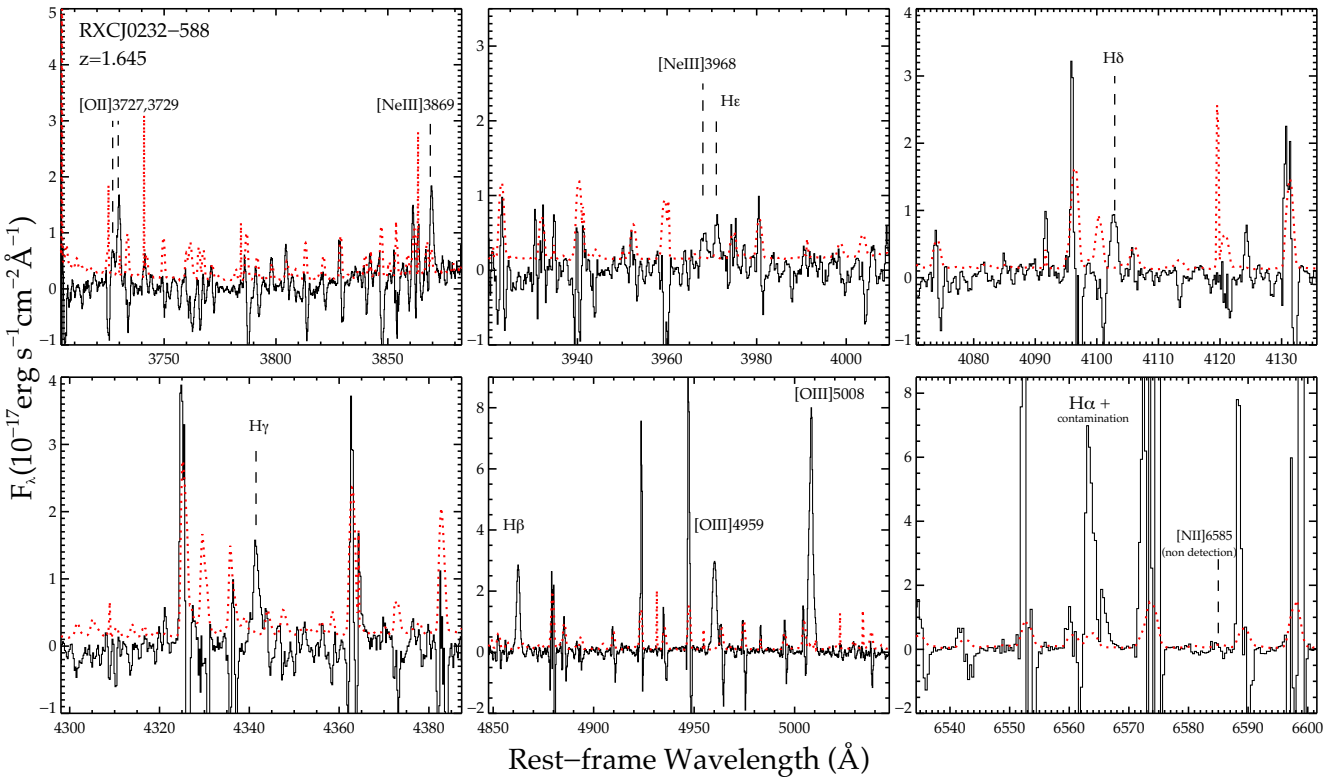

Figure 7. FIRE spectrum of RXCJ0232−588 showing rest-optical emission lines. The black curve represents flux and the red dotted line represents (1σ) uncertainty. The Hα line is contaminated by a skyline. The spectrum reveals several optical emission features sensitive to ionization and abundance (see Section 3.2).

Table 4. Rest-optical emission line measurements of RXCJ0232−588. Emission line fluxes are presented relative to the Hβ. The upper limits are 3σ.

Line	λ_{rest} (Å)	λ_{obs} (Å)	$F_{line}/F_{H\beta}$	EW (Å)
[O II]	3727.13	9857.5	0.24 ± 0.05	59 ± 10
[O II]	3729.92	9864.9	0.34 ± 0.05	41 ± 9
[Ne III]	3869.66	10 235.1	0.52 ± 0.08	91 ± 7
[Ne III]	3968.2	10 494.5	0.16 ± 0.05	28 ± 9
Hϵ	3970.07	10 851.3	0.16 ± 0.05	28 ± 9
Hδ	4102.90	10 851.3	0.24 ± 0.03	46 ± 5
Hγ	4341.58	11 482.6	0.48 ± 0.05	111 ± 12
Hβ	4862.55	12 860.5	1.00	325 ± 23
[O III]	4960.25	13 118.9	1.34 ± 0.03	469 ± 18
[O III]	5008.27	13 245.9	4.08 ± 0.03	1426 ± 57
[N II]	6585	–	<0.08	<77

Note. $F_{H\beta} = (1.52 \pm 0.04) \times 10^{-16}$ erg s^{-1} cm^{-2}.

contributions, we calculate an oxygen abundance of $12 + \log(O/H) = 7.60 \pm 0.24$ (0.08 $Z_\odot$; Asplund et al. 2009). This is 3.5× lower than the direct method oxygen abundance inferred for $z \simeq 2$ galaxies with more typical optical line EWs (e.g. Steidel et al. 2016). We note that the oxygen abundances derived from collisionally excited lines are known to be systematically lower than those derived from faint recombination lines (e.g. Peimbert & Peimbert 2002; Esteban et al. 2014), with the latter thought to be a more reliable measure of the true gas-phase metallicity. However, regardless of the precise absolute value of O/H, the key point we wish to emphasize is that our data imply that RXCJ0232−588 has a significantly lower gas-phase metallicity than is found in the more massive high-redshift star-forming galaxies that have been studied in the MOSDEF and KBSS surveys.

We now consider the ionization state of the gas in RXCJ0232−588. This is often parametrized as a dimensionless ionization parameter ($U = n_\gamma/n_H$), the ratio of the density of hydrogen ionizing photons that are incident on the gas and the number density of hydrogen atoms within the gas. The ionization parameter can be constrained observationally by the ratio of emission lines from the same element with different ionization potentials. Most commonly used is the O32 index, defined as the flux ratio of the [O III] and [O II] doublets. The Ne3O2 index ([Ne III]/[O II]) provides another useful constraint since the Ne/O abundance ratio does not vary substantially with O/H. Over the past several years, the first statistical measures of O32 and Ne3O2 have been obtained at high redshift from the MOSDEF and KBSS surveys (e.g. Shapley et al. 2015; Sanders et al. 2016; Steidel et al. 2016; Strom et al. 2017), revealing evidence for a significantly higher ionization parameter than is common in local H II regions. The trend in redshift could reflect a combination of lower metallicities, harder ionizing spectra, or changes in the geometry of the nebular gas (see Sanders et al. 2016 for a detailed discussion). However, the EELGs we present in this paper are very different from the galaxies in these surveys, with lower stellar masses, large [O III] EWs, lower metallicities, and a stellar population weighted much more towards very massive stars. Recent work has demonstrated that both O32 and Ne3O2 increase with the [O III] EW over 200 Å < $EW_{[O\,III]\lambda5007}$ < 2000 Å (Tang et al. 2019), implying that the gas in the most extreme line emitters is much more highly ionized than in the typical $z \simeq 2$–3 sources discussed earlier.

Table 5. Measured and inferred properties of RXCJ0232−588.

Quantity	Value	Notes
	Electron density-sensitive line ratios	
[O II] 3727/3729	0.75 ± 0.15	$n_e = 80^{+160}_{-60}$ cm^{-3}
	Ionization-sensitive line ratios	
O32	9.39 ± 1.58	[O III] 4959,5008 /[O II] 3727,3729
Ne3O2	0.91 ± 0.19	[Ne III] 3869/[O II] 3727,3729
	Abundance-sensitive line ratios	
N2	<0.03	[N II] 6585/Hα
R23	6.01 ± 0.13	([O III] 4959,5008 + [O II] 3727,3729)/Hβ
	Nebular oxygen abundances (direct method)	
$12 + \log$(O/H)	7.60 ± 0.24	Using auroral line O III] λ1666
	Nebular oxygen abundances (strong line methods)	
$12 + \log(\mathrm{O/H})_{R23}$	7.45 ± 0.05	Using Jones, Martin & Cooper (2015)
$12 + \log(\mathrm{O/H})_{Ne3O2}$	7.84 ± 0.05	Using Jones et al. (2015)
	Inferred gas-phase abundance ratios	
log(C/O)	-0.68 ± 0.19	

Measurements of the ionization-sensitive ratios in RXCJ0232−588 support this picture, revealing nebular gas that is much more highly ionized than in typical $z \simeq 2$–3 galaxies. The O32 ratio (9.39 ± 1.58) is 8× larger than the average of the MOSDEF galaxy sample (Sanders et al. 2016) and 5× larger than is found in the composite spectrum from the KBSS survey (Steidel et al. 2016). The Ne3O2 ratio (0.91 ± 0.19) similarly points to highly ionized gas, with a value that is 6× larger than is found in the KBSS composite (Steidel et al. 2016). The gas conditions in RXCJ0232−588 instead appear very similar to the EELGs presented in Tang et al. (2019), with values of O32 and Ne3O2 that are fully consistent with objects matched by [O III] EW. These results suggest a physical picture whereby the interstellar medium (ISM) in dwarf galaxies is found in a very highly ionized state for a short period following a burst of star formation. Given the frequent association between ionizing photon escape and large O32 (e.g. de Barros et al. 2016; Vanzella et al. 2016b; Izotov et al. 2018; Fletcher et al. 2019), it has been suggested that these bursts may initiate a short window where the ISM is conducive to substantial Lyman continuum leakage in low-mass systems (Tang et al. 2019).

As explained in Section 1, the C/O ratio of the nebular gas is another critical parameter for regulating C III] emission line strengths. While metal-poor star-forming galaxies are often found with sub-solar C/O ratios (Berg et al. 2016, 2019), it has been suggested that solar or super-solar C/O ratios are required to explain the large C III] EWs that have been detected at $z > 6$ if stars are responsible for powering the line emission (e.g. Nakajima et al. 2018). The LDSS spectrum of RXCJ0232−588 allows us to investigate whether this is the case for a system at $z \simeq 2$ with $\mathrm{EW}_{\mathrm{C\,III]}}$ similar to what has been seen in the reionization era. We used PYNEB to calculate the ratio of doubly ionized carbon and oxygen from the flux ratios of C III] and O III] λ1666. To calculate the C/O ratio, we must apply an ionization correction factor (ICF) to C^{2+}/O^{2+}:

$$\frac{C}{O} = \frac{C^{2+}}{O^{2+}} \times \mathrm{ICF}. \quad (2)$$

The ICF accounts for the possibility that volume fraction of C and O in their respective doubly ionized states may not be identical. Berg et al. (2019) have calculated the ICF as a function of the ionization parameter using photoionization models from CLOUDY v17.00 (Ferland et al. 2013). They use BPASS v2.14 burst models (Eldridge & Stanway 2016) with ages ranging between 10^6 and 10^7 yr and stellar metallicities ranging from 0.05 to 0.40 $Z_\odot$. The gas-phase metallicity is taken to be the same as the stars, and the ionization parameter is allowed to vary in the range $-3.0 < \log U < -1.0$. To apply this to RXCJ02232−588, we must first calculate the ionization parameter of the nebular gas. To do so, we use the polynomial fitting functions for $\log U$ presented in Berg et al. (2019). Taking the average value using the coefficients for the $Z = 0.05$ and 0.10 $Z_\odot$ photoionization models and our measured value of O32, we find $\log U = -2.25 \pm 0.14$, where the error bar corresponds to the scatter between the two metallicity models. For this value of $\log U$, we find an ICF of 1.02 ± 0.04 (see Berg et al. 2019), which implies $\log \mathrm{C/O} = -0.68 \pm 0.19$ for the total C/O ratio. This is 0.4× the solar C/O ratio ($\log \mathrm{C/O}_\odot = -0.26$), consistent with the sub-solar values typically found in metal-poor systems in the literature (Garnett et al. 1995; Erb et al. 2010; Christensen et al. 2012; Stark et al. 2014; Berg et al. 2016, 2019; Amorín et al. 2017; Pérez-Montero & Amorín 2017; Senchyna et al. 2017). This suggests that it is possible to power the intense line emission seen in the reionization era with sub-solar C/O ratios.

The ionization and excitation conditions of the nebular gas can be further explored through investigation of the RXCJ0232−588 in the [O III] λ5007/Hβ versus [N II] λ6584/Hα diagnostic diagram (the BPT diagram; Baldwin, Phillips & Terlevich 1981). The flux ratios of RXCJ0232−588 place it in the upper left of the BPT diagram (Fig. 8), in a region consistent with the lines being powered by metal-poor massive stellar populations. The upper limit on N2 ($\log([\mathrm{N\,II}]\ \lambda6584/\mathrm{H}\alpha) < -1.56$) is indicative of low-metallicity gas, as we have shown earlier. The value of O3 ([O III] λ5007/Hβ = 4.08 ± 0.03) is very large, consistent with the gas being both highly ionized and elevated in T_e. While the O3 measurement is somewhat larger than the average value found in the MOSDEF survey (Fig. 8; Sanders et al. 2016), it is nearly identical to that derived from the composite spectrum of KBSS galaxies (Steidel et al. 2016). While the larger ionization parameter of RXCJ0232−588 shifts it towards larger O3, this effect is counterbalanced by the much lower O/H, resulting in an O3 measurement that is similar to that of the less extreme MOSDEF and KBSS galaxies. Recent investigations of Lyman-alpha emitters within the KBSS survey have also revealed many systems with low values of O3 (Trainor et al. 2016), likely

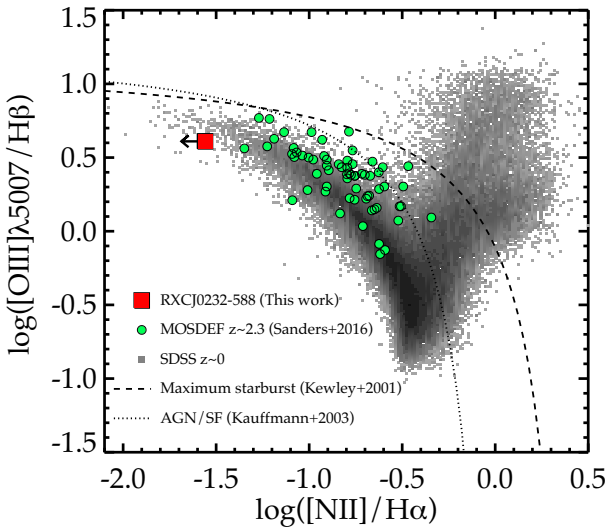

Figure 8. BPT diagram showing the position of RXCJ0232−588 (red square). Grey data points represent $z \sim 0$ SDSS sources. Green circles indicate $z \sim 2.3$ galaxies from the MOSDEF survey. The dashed line depicts the maximum starburst model given by Kewley et al. (2001), whereas the dotted line presents the AGN/SF demarcation from Kauffmann et al. (2003).

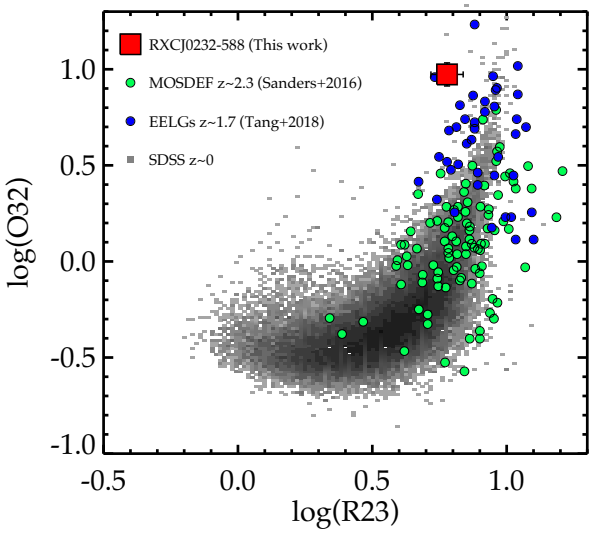

Figure 9. Plot of O32 versus R23 demonstrating the position of RXCJ0232−588 (red square). Grey data points represent $z \sim 0$ SDSS sources. Green circles indicate $z \sim 2.3$ galaxies from the MOSDEF survey and blue circles represent EELGs from Tang et al. (2019).

also reflecting very low gas-phase oxygen abundances. The position of RXCJ0232−588 in the O32 versus R23 diagram (Fig. 9) provides further information on the physical state of the gas. As we motivated earlier, the large O32 of RXCJ0232−588 is consistent with the trend between O32 and [O III] EW presented in the EELG survey of Tang et al. (2019). However, as can be seen in Fig. 9, RXCJ0232−588 has a lower value of R23 (6.01 ± 0.13) than the majority of galaxies with similarly large O32. This is consistent with RXCJ0232−588 having lower metallicity gas than the bulk of the EELGs from the CANDELS fields in Tang et al. (2019), possibly a result of lensing allowing us to probe lower mass galaxies.

One of the key goals in this paper is to ascertain the powering mechanism of the C III] emission in RXCJ0232−588. The data presented here reveal that the ionized gas in the galaxy is metal poor, with an SED that is suggestive of a stellar population weighted towards extremely young stars (see Section 4.2 for model constraints on the age, mass, and sSFR). These properties are very different from C III] emitters with EW > 20 Å presented in Le Fèvre et al. (2019), with lower masses, much younger stellar populations, and no clear signatures of AGN activity. Given the low metallicity of the ionized gas in RXCJ0232−588, we expect the massive stars in the galaxy are likely to power a hard EUV radiation field capable of powering strong nebular line emission. We note that if the stellar metallicity (effectively set by the abundance of iron and iron peak elements) is lower than implied by the gas-phase oxygen abundance due to a delay in iron production (e.g. Steidel et al. 2016; Strom et al. 2018; Sanders et al. 2020), this conclusion will only be strengthened. Given the young age of the stellar population, we also expect a relatively weak underlying optical continuum. The combination of strong nebular emission and weak continuum provides a natural explanation for the extremely large C III] EW seen in the LDSS spectrum of RXCJ0232−588.

While massive stars are likely to provide a large source of EUV photons that contribute to the C III] intensity in RXCJ0232−588, we currently cannot rule out the presence of other sources of ionization. There could be contribution from a narrow-lined AGN (e.g. Feltre et al. 2016; Volonteri et al. 2017), provided it is low enough metallicity to not shift the galaxy away from the upper left of the BPT diagram (e.g. Groves, Heckman & Kauffmann 2006; Izotov & Thuan 2008; Reines, Greene & Geha 2013; Feltre et al. 2016). There also could be contribution from fast radiative shocks (e.g. Allen et al. 2008; Jaskot & Ravindranath 2016), but as with the AGN, we would require the gas to have sufficiently low metallicity for consistency with the low [N II]/Hα ratio (Allen et al. 2008). Constraints on the strength of higher ionization lines in the far-UV (C IV λ1550, He II λ1640) should help disentangle whether shocks or AGNs make a non-negligible contribution to the EUV output (e.g. Feltre et al. 2016; Jaskot & Ravindranath 2016; Mainali et al. 2017), but all current evidence appears consistent with massive stars dominating the ionizing output. In the following section, we will consider whether photoionization from a stellar population alone can self-consistently explain the C III] emission and other spectral constraints in our EELG sample. Failure to do so might already point to the need to consider the alternative sources of ionization described earlier.

4.2 Photoionization modelling

We now investigate the physical properties of the four lensed EELGs in our sample, comparing the observed spectra and photometry to a suite of photoionization models. We make use of the Bayesian galaxy SED modelling and interpreting tool BEAGLE (version 0.20.3; Chevallard & Charlot 2016). BEAGLE is based on photoionization models of star-forming galaxies in Gutkin et al. (2016) that combine the latest version of Bruzual & Charlot (2003) stellar population synthesis models with the photoionization code CLOUDY (Ferland et al. 2013) to calculate emission from star and interstellar gas clouds. Our goals in using BEAGLE are twofold. First, we seek to infer bulk stellar population parameters (i.e. stellar mass, sSFR) implied by the broad-band SED and emission line properties. Secondly, in cases where the spectra are sufficiently constraining, we consider the ionized gas properties required by the data and explore whether stellar photoionization is capable of powering the observed C III] emission.

Table 6. Results from BEAGLE modelling of the four EELGs presented in this paper. From left to right, the columns give the object name, magnification-corrected stellar mass, magnification-corrected SFR, sSFR, ionization parameter, metallicity, stellar age, and *V*-band optical depth.

Object	Stellar mass $[\log(M_\star/\mathrm{M}_\odot)]$	SFR $(\mathrm{M}_\odot\ \mathrm{yr}^{-1})$	sSFR (Gyr^{-1})	Ionization parameter $[\log(U_\mathrm{S})]$	Metallicity $[\log(Z/\mathrm{Z}_\odot)]$	Stellar age (Myr)	$\hat{\tau}_V$
RXCJ0232−588	$7.2^{+0.1}_{-0.1}$	$4.7^{+1.5}_{-1.0}$	$307.0^{+5.1}_{-4.8}$	$-2.06^{+0.05}_{-0.05}$	$-1.21^{+0.02}_{-0.04}$	$3.3^{+0.1}_{-0.1}$	$0.03^{+0.02}_{-0.02}$
RXCJ0911−612	$7.1^{+0.1}_{-0.1}$	$6.2^{+1.2}_{-1.4}$	$491.1^{+291.7}_{-185.1}$	$-2.32^{+0.38}_{-0.32}$	$-1.27^{+0.14}_{-0.18}$	$2.0^{+1.3}_{-0.7}$	$0.18^{+0.12}_{-0.11}$
PLCKG287−5648	$7.3^{+0.2}_{-0.2}$	$1.2^{+0.7}_{-0.5}$	$65.7^{+48.7}_{-26.1}$	$-2.60^{+0.29}_{-0.39}$	$-1.38^{+0.18}_{-0.08}$	$15.2^{+10.0}_{-6.5}$	$0.52^{+0.09}_{-0.10}$
ACTCL0102−4854	$7.9^{+0.1}_{-0.1}$	$4.7^{+1.2}_{-2.1}$	$58.0^{+20.9}_{-13.9}$	$-2.45^{+0.16}_{-0.13}$	$-1.39^{+0.12}_{-0.08}$	$17.2^{+5.5}_{-4.6}$	$0.31^{+0.06}_{-0.06}$

The models allow us to adjust the interstellar metallicity (Z_ISM), the ionization parameter of the HII regions (U_s), here defined at the edge of the Strömgren sphere, and the dust-to-metal ratio (ξ_d), accounting for the depletion of metals on to dust grains. We consider models with a hydrogen density of $n_\mathrm{H} = 100\ \mathrm{cm}^{-3}$. We assume a C/O abundance that is 0.52× that of the solar value [$(\mathrm{C/O})_\odot \approx 0.44$], although we will also explore how models with solar C/O ratios would impact our findings. Our preferred use of a sub-solar C/O ratio is motivated by results demonstrating that galaxies with $12 + \log(\mathrm{O/H}) < 8.0$ tend to have C/O ratios that are less than 0.7× that of solar (e.g. Berg et al. 2019). We showed in Section 4.1 that the UV spectrum of RXCJ0232−588 points towards sub-solar C/O ratios, providing further support for this assumption. We assume a constant star formation history, allowing the maximum stellar age to vary freely between 1 Myr and the age of the Universe at the redshift of the source we are considering. We assume Chabrier (2003) initial mass function and a Calzetti et al. (2000) extinction curve. We consider metallicities in the range of $-2.2 \leq \log(\mathrm{Z/Z})_\odot \leq 0.25$. Similar to our previous work, we assume that the interstellar metallicity is the same as the stellar metallicity ($Z_\star = Z_\mathrm{ISM}$). The redshift of the models is fixed to the spectroscopically determined values for each source. The ionization parameter and dust-to-metal mass ratio are allowed to vary in the range $-4.0 \leq U_\mathrm{S} \leq -1.0$ and $\xi_\mathrm{d} = 0.1$–0.5, respectively.

We fit the broad-band photometry and the emission line EWs simultaneously. The broad-band SED includes seven *HST* filters spanning the optical to near-IR: B_{435}, V_{606}, I_{814}, Y_{105}, J_{125}, JH_{140}, and H_{160}. For one of the four EELGs (RXCJ0911−612), the F555W filter replaces B_{435} and V_{606}. The BEAGLE fits to the photometry and emission line EWs are overlaid on the SEDs in Fig. 2. The model constraints on the magnification-corrected stellar masses, SFRs, dust content ($\hat{\tau}_V$), and sSFRs on the four EELGs are given in Table 6. As can be seen in Fig. 2, the models reproduce the broad-band SEDs. They are also able to reproduce the rest-UV line measurements, and in the case of RXCJ0232−588, they match the rest-optical emission lines (see Table 7).

The stellar masses of the EELGs are very low, ranging from 1.3×10^7 $\mathrm{M}_\odot$ (RXCJ0911−612) to 7.9×10^7 $\mathrm{M}_\odot$ (ACTCL0102−4854). The fits suggest that there is little dust attenuation in these systems ($\hat{\tau}_V = 0.03$–0.52), consistent with the blue UV continuum slopes that we observed in the broad-band data (Section 3.1). As expected, we find that the sSFRs are very large and broadly increase with the amplitude of the J_{125}-band excess, ranging from 58 Gyr^{-1} (ACTCL0102−4854) and 66 Gyr^{-1} (PLCKG287−5648) to 310 Gyr^{-1} (RXCJ0232−588) and 490 Gyr^{-1} (RXCJ0911−612). These sSFRs imply very young mean stellar ages ($\lesssim$20 Myr) for the assumed constant star formation history. The young stellar age reflects that a recent burst dominates the observed SED and may not necessarily imply absence of faint older stellar populations from a past star formation activity. Under an assumption that the star formation proceeded with a recent burst on top of an evolved stellar population, we found that the stellar age of oldest stars could be several hundred Myr. For instance, in case of RXCJ0232−588 when we assume a recent burst within the last 5 Myr along with the presence of evolved stars (represented by a delayed star formation history), we found that the maximum stellar age could be as high as 260 Myr. We note that the composite stellar population model increases our stellar mass estimates by 0.5 dex, since this takes into account older generation of stars in the galaxy. However, the implied age of the recent burst is still low (1.6 Myr). It is only at these young ages that the ratio of O to A stars is large enough to reproduce the large EW optical line emission. The ages range from 2.0 and 3.3 Myr for RXCJ0911−612 and RXCJ0232−588 to 15 and 17 Myr for PLCKG287−5648 and ACTL0102−4854. At ages of less than 3 Myr, the O star population will not have had time to equilibrate and will be weighted more strongly to the hottest O stars, resulting in a harder EUV spectrum. We thus expect the models that reproduce RXCJ0911−612 and RXCJ0232−588 will have harder ionizing spectra than those of the other EELGs in our sample.

Table 7. Observed and BEAGLE predicted emission line properties of the galaxies presented in this paper. The model values represent the posterior median of the marginal posterior distribution.

Object	Quantity	Data	Model
RXCJ0232−588	C III] EW (Å)	21.7 ± 2.8	20.5
	O32	9.39 ± 3.10	11.85
	R23	6.01 ± 2.06	6.47
	[O III] λ5007/H β	4.09 ± 0.56	4.47
	[O III] λ5007 EW (Å)	1426 ± 156	1692
RXCJ0911−612	C III] EW (Å)	16.9 ± 3.2	15.9
PLCKG287−5648	C III] EW (Å)	4.8 ± 1.1	4.9
ACTCL0102−4854	C III] EW (Å)	<4.0	3.8
	[O II] EW (Å)	59.2 ± 5.7	54.2

In the case of RXCJ0232−588, the rest-UV and optical spectra have enough emission line detections to enable characterization of the ionized gas properties. For our assumed sub-solar C/O ratio, the implied metallicity is very low ($\log Z/\mathrm{Z}_\odot = -1.21^{+0.02}_{-0.04}$), the dust attenuation is minimal ($\hat{\tau}_V = 0.03^{+0.02}_{-0.02}$), and the ionization parameter is large ($\log U_\mathrm{S} = -2.06^{+0.05}_{-0.05}$). These parameters are capable of reproducing the optical line ratios and C III] EW within observational uncertainties (Table 7), and we note that the metallicity implied by the photoionization modelling (0.06 ± 0.01 $\mathrm{Z}_\odot$) is fully consistent with that implied by the T_e analysis in Section 4.1 (0.08 ± 0.03 $\mathrm{Z}_\odot$). We also consider models with C/O ratios consistent with the solar value. In this case, the derived properties remain very similar, but the model C III] EW (29 Å) significantly exceeds the value determined observationally, providing additional support for a sub-solar C/O ratio. We thus find that there are viable

sets of parameters (i.e. metallicity, age, ionization parameter) that can reproduce the large C III] EW of RXCJ0232−588 with stellar photoionization. The BEAGLE modelling procedure suggests that such strong UV metal lines are a natural by-product of the radiation field and gas conditions associated with an extremely young (3 Myr) and low-metallicity (0.06 $Z_{\odot}$) stellar population, as might expected to appear during a burst of star formation. While we cannot rule out other sources of ionization, the mere detection of C III] with EW > 20 Å should not necessarily imply the presence of AGNs.

For RXCJ0911−612, we do not have a rest-optical spectrum, but the detection of strong C III] together with the pronounced J_{125}-band excess is already enough to place some constraints on the range of gas properties that can reproduce the data. When we adopt the sub-solar C/O models, we find that the data prefer low metallicity ($\log Z/Z_{\odot} = -1.27^{+0.14}_{-0.18}$), minimal dust attenuation ($\hat{\tau}_V = 0.18^{+0.12}_{-0.11}$), and a large ionization parameter ($\log U_S = -2.32^{+0.38}_{-0.32}$). Not surprisingly, these properties are very similar to those derived for RXCJ0232−588, although the uncertainties in the gas properties of RXCJ0911−612 are considerably larger, owing to the absence of rest-optical line constraints. Nonetheless, all evidence points towards the observations being consistent with another young system dominated by low-metallicity massive stars. We are unable to usefully constrain the ionized gas properties for the two objects where the rest-UV lines are weak (or undetected) and rest-optical spectroscopy is not yet available (PLCKG287−5648 and ACTCL0102−4854). While the broad-band SED suggests that these systems are slightly older than the two systems described earlier (Table 6), it is not clear whether the metallicity or ionization parameter is significantly different. Near-IR spectroscopy will be required to usefully constrain the gas conditions, providing a complete explanation as to why these systems power weaker C III] emission.

5 DISCUSSION

The spectroscopic study of reionization-era galaxies is one of the primary science drivers behind the development of near-IR spectrographs for the current and future generation of optical/IR telescopes. Whereas *JWST* will be able to detect strong rest-optical nebular lines such as [O III] and H β from $z > 6$ galaxies, ground-based optical/IR facilities will be limited to the spectral features within the rest-UV. Identifying the optimal spectral features in the UV is particularly important for our ability to spectroscopically study the large sample of $z > 6$ galaxies that will be identified photometrically by future imaging campaigns, for example with the *Wide Field Infrared Survey Telescope* (*WFIRST*), as the areas covered will be much too wide for *JWST* follow-up.

The discovery of intense UV metal line emission in $z > 6$ galaxies suggests a path towards achieving this goal. While the faint lines are a challenge for existing facilities, their detection will become much easier with upcoming 25–40 m class telescopes, potentially opening the door for C III] and C IV to be used for large redshift surveys in the reionization era. However, it is worth emphasizing that we are currently very far from this goal. Each of the $z > 6$ UV metal line detections are associated with relatively bright galaxies ($H < 26$) for which the redshift was already known from Ly α emission; efforts to target C III] in galaxies lacking spectroscopic confirmation have proven extremely challenging for current facilities (e.g. Zitrin et al. 2015). Focusing on galaxies with Ly α redshifts is a natural starting place for the demonstration of method, but this approach almost certainly leads to a biased spectroscopic sample, including only those sources in large enough ionized regions of the intergalactic medium for Lyα to be detectable at $z > 7$.

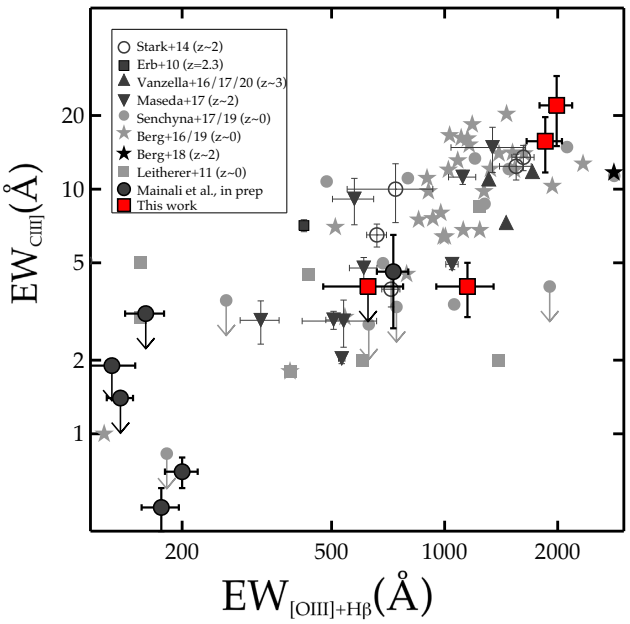

Figure 10. Plot of C III] rest-frame EW ($EW_{C\,III]}$) as a function of [O III] + H β rest-frame EW ($EW_{[O\,III]+H\beta}$). The red square represents data presented in this paper. The plot also includes a data compilation from the literature (Erb et al. 2010; Leitherer et al. 2011; Stark et al. 2014, 2017; Berg et al. 2016; Vanzella et al. 2016a, 2017, 2020; Senchyna et al. 2017).

The last few years have seen several key steps taken towards the eventual use of C III] and other faint UV lines as the primary means of spectroscopic confirmation at $z > 6$. Most importantly, we have improved our understanding of the stellar populations and gas conditions that support the strong line emission we are now seeing at $z > 6$ (e.g. Stark et al. 2014; Rigby et al. 2015; Du et al. 2017; Senchyna et al. 2017). Intense metal line emission is found in galaxies that are both metal poor ($\lesssim$0.4 $Z_{\odot}$ for C III]; Senchyna et al. 2017) and dominated by very young stellar populations. The latter trend is most clearly seen in the relation between C III] EW and the [O III] or H β EWs. In Fig. 10, we present an updated compilation of the dependence of the C III] EW on the [O III] + H β EW. With the inclusion of the sources from our survey, it is now apparent that the C III] EW reaches the values seen at $z > 6$ ($EW_{C\,III]} > 20$ Å) in a subset of sources with [O III] + H β EW $\simeq$ 2000 Å. In the context of the photoionization models discussed in Section 4.2, the C III] detections at $z > 6$ imply extremely young stellar populations expected within several Myr after a burst of star formation.

This relationship guides the survey strategy for targeting C III] as the primary redshift indicator in metal-poor star-forming galaxies. The results of this paper demonstrate the feasibility of such efforts. The sources we have targeted lacked spectroscopic confirmation but showed photometric flux excesses indicative of intense [O III] + H β emission at $z \simeq 1.6$–1.8. We were able to spectroscopically confirm the redshifts of the sources with the three largest broad-band flux excess (i.e. the largest [O III] + H β EWs) through detection of C III] emission. These are among the first sources at high redshift for which C III] was used as the primary means of spectroscopic confirmation. In each case, we guided our spectroscopic exposure times by expectations from the relationship between C III] EW and [O III] + H β EW seen in Fig. 10.

The success of this approach motivates a renewed focus on current efforts to use C III] as a redshift probe for reionization-era galaxy candidates. The *Spitzer*/IRAC imaging necessary to identify intense rest-optical line emission is now available over large areas (e.g. de Barros et al. 2019; Stefanon et al. 2019; Strait et al. 2020), allowing efficient selection of bright galaxies likely to have detectable C III] emission. In particular, Fig. 10 suggests that identification of sources with C III] EW in excess of 10–20 Å requires pre-selecting those galaxies with broad-band flux excesses implying an [O III] + Hβ EW above 1500 Å. As discussed in Section 1, this [O III] + Hβ EW is not typical of galaxies in the reionization era, corresponding to roughly twice the value implied by composite SEDs (Labbé et al. 2013). However, by limiting spectroscopic searches to this subset of intense optical line emitters, it should be possible to efficiently identify C III] emission independently of Lyα in deep near-IR spectra. In the era of the ELTs, these surveys can be extended to more typical sources with less extreme [O III] + Hβ EWs. With spectroscopic flux limits expected from the ELTs (e.g. Papovich et al. 2019), the relationship in Fig. 10 suggests that it should be possible to identify C III] in typical galaxies down to $H \simeq 26$–27, thereby providing one of the only means of building large redshift samples at $z > 6$ from future imaging surveys conducted by *WFIRST* and other wide-area near-IR missions, opening new doors for insight into early galaxies and reionization.

6 SUMMARY

The detection of intense C III] and C IV emission in the spectra of $z > 6$ galaxies has proven challenging to interpret. Some have suggested that AGNs may be required to power the line emission (e.g. Nakajima et al. 2018), whereas others have suggested that the radiation field from young metal-poor stellar populations is sufficient (Stark et al. 2017). The difficulty stems in part from our poor understanding of the EUV radiation field powered by low-metallicity stellar populations. Without an improved reference sample of UV nebular line spectra of metal-poor galaxies at lower redshifts, it will be impossible to distinguish between these two pictures.

With the aim of beginning to assemble such a sample at $z \simeq 2$, we have obtained Magellan/IMACS and LDSS spectra targeting C III] in four gravitationally lensed reionization-era analogues identified in *HST* imaging of cluster fields from the RELICS. The galaxies were selected to have a flux excess in the J_{125} band, indicative of strong [O III] + Hβ emission (EW = 500–2000 Å), similar to what has been inferred from the SEDs of the $z > 6$ galaxies with C III] detections. Our goal is to improve our understanding of the stellar populations and gas physical conditions that are required to power the intense C III] emission that has been observed at $z > 6$. We summarize our main findings below.

(1) We detect C III] emission in three out of the four EELGs in our sample, with the EW of C III] scaling with the [O III] + Hβ EW. The two objects with the largest [O III] + Hβ EWs are found to have C III] strengths approaching those seen at $z > 6$ ($EW_{C\,III]} \simeq$ 17-22 Å). These results suggest that the relationship between C III] EW and [O III] EW continues well into the EELG regime, with the intense C III] emission seen at $z \gtrsim 6$ linked to the most intense optical line emitters ($EW_{[O\,III]+H\beta}$ >1500-2000 Å).

(2) Each of the four lensed galaxies in our sample are characterized by very low stellar masses (1.3–7.9 $\times$ 10^7 $M_\odot$), large sSFRs (58–490 Gyr^{-1}), and low dust attenuation (V-band optical depth $\hat{\tau}_V = 0.0$–0.5), consistent with a population of dwarf galaxies that have recently undergone a burst of star formation. The broad-band SED and extreme optical line emission imply very young luminosity-weighted ages (for a constant star formation history), ranging from 2–3 Myr for the most extreme line emitters to 15–20 Myr for the two EELGs with less prominent [O III] + Hβ emission.

(3) We have obtained a Magellan/FIRE near-IR spectrum of RXCJ0232−588, providing insight into the gas conditions in one of the only low-mass galaxies known at $z \simeq 0$–2 with an integrated C III] EW as large as at $z > 6$ ($EW_{C\,III]} > 20$ Å). We find that the galaxy is very metal poor ($12 + \log(O/H) = 7.6 \pm 0.2$) with a highly ionized ISM (O32 = 9.39) and a sub-solar C/O ratio ($\log C/O = -0.68$). The properties of the source are very different from previously known C III] emitters with EW > 20 Å at $z \simeq 2$–3 (Le Fèvre et al. 2019), each of which have shown super-solar C/O ratios or evidence for AGN activity. Instead, these properties appear to be very similar to recent studies of metal-poor low-mass galaxies at similar redshifts (Vanzella et al. 2016a, 2017; Amorín et al. 2017; Berg et al. 2018).

(4) We fit the emission lines and broad-band SEDs of the EELGs in our sample using the BEAGLE photoionization modelling tool (Chevallard & Charlot 2016). We find that stars are capable of powering the observed C III] emission without contribution from additional sources of ionization (AGNs, shocks), in spite of the sub-solar C/O ratio. In particular, the EUV radiation field associated with a young (2–3 Myr), metal-poor stellar population (0.05–0.06 $Z_\odot$) is able to simultaneously reproduce the C III] emission, optical nebular line ratios, and broad-band SED in our sample of extreme line emitters. In this context, the increased detection rate of intense C III] emission at $z > 6$ (Mainali et al. 2018) may suggest that such young, metal-poor stellar populations are becoming more common in the reionization era.

(5) The three UV line emitters in our sample are among the first sources for which C III] was successfully used as the primary means of redshift confirmation. We discuss implications for the use of C III] as a spectroscopic tool in the reionization era, arguing that the relationship between C III] EW and [O III] EW should already make it feasible to confirm redshifts of $z > 6$ carefully selected galaxies that have yet to be confirmed via Lyα. In particular, $z \simeq 7$–8 dropouts with *Spitzer*/IRAC flux excesses indicative of $EW_{[O\,III]+H\beta}$ >1500-2000 Å are likely to have prominent C III] emission, making spectroscopic confirmation tractable in sufficiently bright galaxies. In the era of the ELTs, it should be feasible to detect C III] in less extreme sources, providing one of the most efficient means of redshift confirmation for photometric sources identified in *WFIRST* imaging.

ACKNOWLEDGEMENTS

We thank Xinnan Du, Anna Feltre, Taylor Hutchison, Alice Shapley, and Casey Papovich for helpful discussions. DPS acknowledges support from the National Science Foundation through the grant AST-1410155. This paper includes data gathered with the 6.5 m Magellan Telescopes located at Las Campanas Observatory, Chile. This work is based on observations taken by the RELICS Treasury Program (GO-14096) with the NASA/ESAHST. Program GO-14096 is supported by NASA through a grant from the Space Telescope Science Institute, which is operated by the Association of Universities for Research in Astronomy, Inc., under NASA contract NAS5-26555. The paper uses high level science products (HLSP) from the RELICS program, including catalogues and lens

models, which were retrieved from the Mikulski Archive for Space Telescopes (MAST).

REFERENCES

Acebron A. et al., 2018, ApJ, 858, 42
Alavi A. et al., 2016, ApJ, 832, 56
Allen M. G., Groves B. A., Dopita M. A., Sutherland R. S., Kewley L. J., 2008, ApJS, 178, 20
Amorín R. et al., 2014, A&A, 568, L8
Amorín R. et al., 2017, Nat. Astron., 1, 0052
Asplund M., Grevesse N., Sauval A. J., Scott P., 2009, ARA&A, 47, 481
Atek H. et al., 2011, ApJ, 743, 121
Baldwin J. A., Phillips M. M., Terlevich R., 1981, PASP, 93, 5
Berg D. A., Skillman E. D., Henry R. B. C., Erb D. K., Carigi L., 2016, ApJ, 827, 126
Berg D. A., Erb D. K., Auger M. W., Pettini M., Brammer G. B., 2018, ApJ, 859, 164
Berg D. A., Erb D. K., Henry R. B. C., Skillman E. D., McQuinn K. B. W., 2019, ApJ, 874, 93
Bouwens R. J. et al., 2015a, ApJ, 803, 34
Bouwens R. J., Illingworth G. D., Oesch P. A., Caruana J., Holwerda B., Smit R., Wilkins S., 2015b, ApJ, 811, 140
Bradley L. D. et al., 2014, ApJ, 792, 76
Bruzual G., Charlot S., 2003, MNRAS, 344, 1000
Byler N., Dalcanton J., Conroy C., Johnson B., Levesque E., Berg D., 2018, ApJ, 863, 14
Calzetti D., Armus L., Bohlin R. C., Kinney A. L., Koornneef J., Storchi-Bergmann T., 2000, ApJ, 533, 682
Cerny C. et al., 2018, ApJ, 859, 159
Chabrier G., 2003, PASP, 115, 763
Chevallard J., Charlot S., 2016, MNRAS, 462, 1415
Christensen L. et al., 2012, MNRAS, 427, 1953
Cibirka N. et al., 2018, ApJ, 863, 145
Coe D. et al., 2019, ApJ, 884, 85
Curtis-Lake E. et al., 2016, MNRAS, 457, 440
de Barros S. et al., 2016, A&A, 585, A51
de Barros S., Oesch P. A., Labbé I., Stefanon M., González V., Smit R., Bouwens R. J., Illingworth G. D., 2019, MNRAS, 489, 2355
Dressler A. et al., 2011, PASP, 123, 288
Du X., Shapley A. E., Martin C. L., Coil A. L., 2017, ApJ, 838, 63
Du X. et al., 2018, ApJ, 860, 75
Eldridge J. J., Stanway E. R., 2016, MNRAS, 462, 3302
Erb D. K., Pettini M., Shapley A. E., Steidel C. C., Law D. R., Reddy N. A., 2010, ApJ, 719, 1168
Esteban C., García-Rojas J., Carigi L., Peimbert M., Bresolin F., López-Sánchez A. R., Mesa-Delgado A., 2014, MNRAS, 443, 624
Feltre A., Charlot S., Gutkin J., 2016, MNRAS, 456, 3354
Ferland G. J. et al., 2013, Rev. Mex. Astron. Astrofis., 49, 137
Finkelstein S. L. et al., 2013, Nature, 502, 524
Finkelstein S. L. et al., 2015, ApJ, 810, 71
Finkelstein S. L. et al., 2019, ApJ, 879, 36
Fletcher T. J., Tang M., Robertson B. E., Nakajima K., Ellis R. S., Stark D. P., Inoue A., 2019, ApJ, 878, 87
Garnett D. R., Skillman E. D., Dufour R. J., Peimbert M., Torres-Peimbert S., Terlevich R., Terlevich E., Shields G. A., 1995, ApJ, 443, 64
González V., Bouwens R., Illingworth G., Labbé I., Oesch P., Franx M., Magee D., 2014, ApJ, 781, 34
Groves B. A., Heckman T. M., Kauffmann G., 2006, MNRAS, 371, 1559
Gutkin J., Charlot S., Bruzual G., 2016, MNRAS, 462, 1757
Hainline K. N., Shapley A. E., Greene J. E., Steidel C. C., 2011, ApJ, 733, 31
Hashimoto T. et al., 2018, Nature, 557, 392
Hu W. et al., 2017, ApJ, 845, L16
Hutchison T. A. et al., 2019, ApJ, 879, 70
Izotov Y. I., Thuan T. X., 2008, ApJ, 687, 133
Izotov Y. I., Worseck G., Schaerer D., Guseva N. G., Thuan T. X., Fricke Verhamme A., Orlitová I., 2018, MNRAS, 478, 4851
Jaskot A. E., Ravindranath S., 2016, ApJ, 833, 136
Jones T., Martin C., Cooper M. C., 2015, ApJ, 813, 126
Kauffmann G. et al., 2003, MNRAS, 346, 1055
Kelson D. D., 2003, PASP, 115, 688
Kewley L. J., Dopita M. A., Sutherland R. S., Heisler C. A., Trevena J., 2001, ApJ, 556, 121
Labbé I. et al., 2013, ApJ, 777, L19
Laporte N., Nakajima K., Ellis R. S., Zitrin A., Stark D. P., Mainali R., Roberts-Borsani G. W., 2017, ApJ, 851, 40
Le Fèvre O. et al., 2019, A&A, 625, A51
Leitherer C., Tremonti C. A., Heckman T. M., Calzetti D., 2011, AJ, 141, 37
Livermore R. C., Finkelstein S. L., Lotz J. M., 2017, ApJ, 835, 113
Luridiana V., Morisset C., Shaw R. A., 2015, A&A, 573, A42
McLure R. J. et al., 2013, MNRAS, 432, 2696
Mainali R., Kollmeier J. A., Stark D. P., Simcoe R. A., Walth G., Newman A. B., Miller D. R., 2017, ApJ, 836, L14
Mainali R. et al., 2018, MNRAS, 479, 1180
Maseda M. V. et al., 2014, ApJ, 791, 17
Mollá M., García-Vargas M. L., Bressan A., 2009, MNRAS, 398, 451
Nakajima K. et al., 2018, A&A, 612, A94
Ono Y. et al., 2012, ApJ, 744, 83
Ono Y. et al., 2013, ApJ, 777, 155
Osterbrock D. E., Ferland G. J., 2006, Astrophysics of Gaseous Nebulae and Active Galactic Nuclei. University Science Books, Mill Valley, CA
Papovich C. et al., 2019, Bull. Am. Astron. Soc., 51, 266
Paterno-Mahler R. et al., 2018, ApJ, 863, 154
Peimbert M., Peimbert A., 2002, in Clariá J. J., García Lambas D., Levato H., eds, Revista Mexicana de Astronomia y Astrofisica Conference Series. Proc. Rev. Mex. Astron. Astrofis. Conf. Ser. Vol. 14, p. 47, X Reunión Regional Latinoamericana de Astronomía, IAU
Pérez-Montero E., 2017, PASP, 129, 043001
Pérez-Montero E., Amorín R., 2017, MNRAS, 467, 1287
Reines A. E., Greene J. E., Geha M., 2013, ApJ, 775, 116
Rigby J. R., Bayliss M. B., Gladders M. D., Sharon K., Wuyts E., Dahle H., Johnson T., Peña-Guerrero M., 2015, ApJ, 814, L6
Robertson B. E. et al., 2013, ApJ, 768, 71
Salmon B. et al., 2015, ApJ, 799, 183
Sanders R. L. et al., 2016, ApJ, 816, 23
Sanders R. L. et al., 2020, MNRAS, 491, 1427
Schmidt K. B. et al., 2017, ApJ, 839, 17
Senchyna P. et al., 2017, MNRAS, 472, 2608
Senchyna P., Stark D. P., Chevallard J., Charlot S., Jones T., Vidal García A., 2019, MNRAS, 488, 3492
Shapley A. E., Steidel C. C., Pettini M., Adelberger K. L., 2003, ApJ, 588, 65
Shapley A. E. et al., 2015, ApJ, 801, 88
Simcoe R. A. et al., 2013, PASP, 125, 270
Smit R. et al., 2014, ApJ, 784, 58
Smit R. et al., 2015, ApJ, 801, 122
Stanway E. R., Eldridge J. J., Becker G. D., 2016, MNRAS, 456, 485
Stark D. P., 2016, ARA&A, 54, 761
Stark D. P., Schenker M. A., Ellis R., Robertson B., McLure R., Dunlop J., 2013, ApJ, 763, 129
Stark D. P. et al., 2014, MNRAS, 445, 3200
Stark D. P. et al., 2015a, MNRAS, 450, 1846
Stark D. P. et al., 2015b, MNRAS, 454, 1393
Stark D. P. et al., 2017, MNRAS, 464, 469
Stefanon M. et al., 2019, ApJ, 883, 99
Steidel C. C., Strom A. L., Pettini M., Rudie G. C., Reddy N. A., Trainor R. F., 2016, ApJ, 826, 159
Strait V. et al., 2020, ApJ, 888, 124
Strom A. L., Steidel C. C., Rudie G. C., Trainor R. F., Pettini M., Reddy N. A., 2017, ApJ, 836, 164
Strom A. L., Steidel C. C., Rudie G. C., Trainor R. F., Pettini M., 2018, ApJ, 868, 117

Tang M., Stark D. P., Chevallard J., Charlot S., 2019, MNRAS, 489, 2572
Tilvi V. et al., 2016, ApJ, 827, L14
Trainor R. F., Strom A. L., Steidel C. C., Rudie G. C., 2016, ApJ, 832, 171
van der Wel A. et al., 2011, ApJ, 742, 111
Vanzella E. et al., 2016a, ApJ, 821, L27
Vanzella E. et al., 2016b, ApJ, 825, 41
Vanzella E. et al., 2017, ApJ, 842, 47
Vanzella E. et al., 2020, MNRAS, 491, 1093
Volonteri M., Reines A. E., Atek H., Stark D. P., Trebitsch M., 2017, ApJ, 849, 155
Zitrin A. et al., 2015, ApJ, 810, L12
Zitrin A. et al., 2017, ApJ, 839, L11

This paper has been typeset from a TEX/LATEX file prepared by the author.